

**Effect of V_2O_5 Addition on the Structural, Magnetic and Electrical
Properties of Ni-Co-Zn Ferrites**

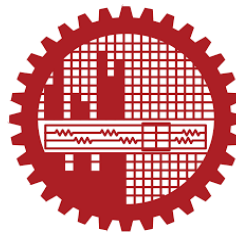
A dissertation submitted to the Department of Physics, Bangladesh University of
Engineering & Technology in partial fulfillment of MASTER OF SCIENCE in
PHYSICS

by

Md. Firoz Uddin

Student ID: 1017142509

Session: October 2017



Department of Physics

BANGLADESH UNIVERSITY OF ENGINEERING AND TECHNOLOGY

September, 2020



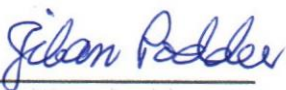
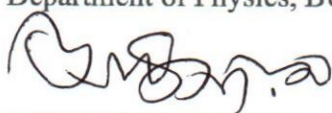

BANGLADESH UNIVERSITY OF ENGINEERING & TECHNOLOGY (BUET), DHAKA
DEPARTMENT OF PHYSICS



Certification of Thesis work

The thesis titled “EFFECT OF V_2O_5 ADDITION ON THE STRUCTURAL, MAGNETIC AND ELECTRICAL PROPERTIES OF Ni-Co-Zn FERRITES” submitted by **Md. Firoyz Uddin**, Roll No.1017142509F, Session: October/2017 has been accepted as satisfactory in partial fulfillment of the requirement for the degree of **Master of Science (M.Sc.)** in Physics on 5th September, 2020.

BOARD OF EXAMINERS

1. 
Dr. Muhammad Samir Ullah (Supervisor) Chairman
Associate Professor
Department of Physics, BUET, Dhaka
2. 
Dr. Md. Rafi Uddin Member
Head and Professor (Ex-Officio)
Department of Physics, BUET, Dhaka
3. 
Dr. Jiban Podder Member
Professor
Department of Physics, BUET, Dhaka.
4. 
Dr. Mohammad Abu Sayem Karal Member
Associate Professor
Department of Physics, BUET, Dhaka.
5. 
Dr. Golam Mohammed Bhuiyan Member
Professor (External)
Department of Theoretical Physics
University of Dhaka, Dhaka.

CANDIDATE'S DECLARATION

It is hereby declared that this thesis or any part of it has not been submitted elsewhere for the award of any degree or diploma.

Md. Firoz Uddin

Dedicated to

My Parents: Md. Abdus Salam & Most. Firoza Begum

and

All of my Teachers

Acknowledgements

All praise for Allah who has created us and given a greatest status among his all creations. I am so grateful to almighty Allah for giving me strength, courage, patience and ability to complete this study.

Firstly, I would like to express my deepest sense of gratitude and pleasure thanks to my supervisor **Dr. Muhammad Samir Ullah**, Associate professor, Department of Physics, Bangladesh University of Engineering and Technology (BUET), Dhaka-1000, for his scholastic supervision, valuable guidance and helpful discussion throughout the progress of this work. I am highly grateful to him for allowing me to conduct independent research.

I am extremely grateful to Prof. Dr. Md. Rafi Uddin, Head, Department of Physics, BUET, Dhaka-1000, for kindly permitting me to carry out this research in the Physics Laboratory and to the BUET authorities for providing the necessary financial grant for the research. I am extremely grateful Dr. Sheikh Manjura Hoque, Head, Material Science Division, Atomic Energy Centre Dhaka, Dhaka-1000, for her cooperation during my research work. Also, I am extremely grateful Dr. M. A. Hakim, Department of Glass and Ceramics Engineering, BUET, Dhaka-1000, for her cooperation during my research work. I would like to express my gratitude to Prof. Dr. Jiban Podder, Prof. Dr. Md. Feroz Alam Khan, Prof. Dr. A. K. M. Akther Hossain, Prof. Dr. Mostak Hossain, Prof. Dr. Afia Begum, Prof. Dr. Forhad Mina, Prof. Dr. Nasreen Akter, Prof. Dr. Mohammed Abdul Basith, Dr. Mohammad Abu Sayem Karal, Dr. Mohammad Jellur Rahman, Dr. Muhammad Rakibul Islam, Dr. Muhammad Khurshed Alam, Dr. Md. Azizar Rahman, Dr. Mehnaz Sharmin and A.T.M. Shafiul Azam , Dr. Parvin Sultana, Department of Physics, BUET for their sincere cooperation.

Most importantly, I would like to extent my gratitude to my family members, especially my parents and my elder sister Mst. Najma Begum for their love, support and blessings, who have always been the greatest inspiration in my life in every possible way. I wish to thank specially Zhorna Begum, Mahmudul Hasan, Md. Zahidur Rahman, S. M. Rubaytul Islam, Rowson Satara, Tanzila Tasnim, Jakiul Islam for their constant support.

ABSTRACT

The effect of V_2O_5 addition on the structural, magnetic and electrical properties of Ni-Co-Zn ferrites having the compositions $Ni_{0.62}Co_{0.03}Zn_{0.35}Fe_2O_4 + xV_2O_5$ (where $x=0.0, 0.5, 1.0$ and $1.5\text{wt}\%$) are reported. The samples were prepared by solid state reaction and sintered at 1200°C . The crystalline structure of all the samples showed cubic spinel structure. The microstructural study reveals that the grain growths of Ni-Co-Zn mixed ferrites are strongly depended on the amount of V_2O_5 contents. The saturation magnetization (M_S) and coercivity (H_C) were determined from the magnetic hysteresis loops, while Curie temperatures (T_C) were estimated from the temperature dependence of magnetization. The M_S almost linearly decreased from 77emu/g for $x=0.0\text{ wt}\% V_2O_5$ to 56.5 emu/g for $x=1.5\text{wt}\% V_2O_5$. Similarly, T_C for the studied samples gradually decreased with increase of V_2O_5 addition upto $x=1.0\text{ wt}\% V_2O_5$ and displayed an upturn at $x=1.5\text{ wt}\% V_2O_5$. A general termed of permeability enhancement is clearly evidenced on V_2O_5 addition. The dielectric constant and dielectric loss factor were measured for all the samples as a function of frequency at room temperature. The variation of ac resistivity with applied frequency was also measured at room temperature. The ac resistivity decreases with increasing of frequency and then it remains constant at higher frequency for all the compositions.

Contents

Abstract	vi
Contents	vii
List of Figures	ix
List of Table	xii
List of Abbreviation	Xiii
Chapter 1: Introduction	1-5
1.1 Spinel Ferrites	1
1.2 Motivation	2
1.3 Objectives of the present study	4
1.4 Outline of the Thesis	5
Chapter 2: Literature view and Theoretical Aspects	6-24
2.1 Literature Review	6
2.2 Theoretical Aspects	10
2.2.1 Magnetism in Solids	10
2.2.2 Magnetic ordering	12
2.2.3 Ferrites	14
2.2.4 Exchange Interaction in the Spinel Ferrites	17
2.2.5 The Two Sub-lattice Model	18
2.2.6 Hysteresis loop	21
2.2.7 Maxwell-Wagner Polarization Mechanism	22
Chapter 3: Samples Preparation and Characterizations	25-56
3.1 Samples Preparation	25
3.1.1 Raw Materials	25
3.1.2 Solid State Reaction Method	28
3.1.3 Calcining, Pressing and Sintering	32
3.1.4 Etching	37
3.1.5 Preparation of the Present Samples	38
3.2 Characterization	39
3.2.1 The X-ray Diffraction	39
3.2.2 Interpretation of the XRD Data	41
3.2.3 X- Ray density and bulk density determination	42

3.2.4 The Study of Field Emission Scanning Electron Microstructure	42
3.2.5 Energy-Dispersive X-ray Spectroscopy	44
3.2.6 Curie Temperature (T_c) Measurement	45
3.2.7 Saturation Magnetization Measurement	46
3.2.8 Complex Permeability Measurement	48
3.2.9 Electrical Resistivity Measurement	53
3.2.10 Dielectric constant measurement	53
3.2.11 Impedance spectroscopy	54
Chapter 4: Results and Discussion	57-81
4.1 Structural Property of V_2O_5 added Ni-Co-Zn ferrites	57
4.1.1 X-ray Diffraction	57
4.2 Surface Morphology	62
4.3 Elemental Analysis	63
4.4 Magnetic Properties	66
4.4.1 M-H curve at room temperature	66
4.4.2 M-H curve at different Temperatures	68
4.4.3 Curie Temperature	70
4.5 Complex Permeability	72
4.6 Electrical Properties	75
4.6.1 Dielectric Constant	75
4.6.2 Dielectric loss tangent	77
4.6.3 AC Resistivity	78
4.6.4 Complex Impedance Spectroscopy	79
Chapter 5: Conclusions	82-84
References	

List of Figures

Fig.2.1 Temperature dependence of the inverse susceptibility for:(a) a diamagnetic material; (b) a paramagnetic material, showing Curie's law behavior; (c) a ferromagnetic material, showing a spontaneous magnetization for $T < T_C$ and Curie – Weiss behavior for $T > T_C$ (d) and antiferromagnetic material; (e) a ferrimagnetic material, showing a net spontaneous magnetization for $T < T_C$ and non-linear behaviour for $T > T_C$.

Fig.2.2 Unit cell of Cubic ferrite.

Fig.2.3 Inter ionic angles for the different type of lattice site interactions.

Fig.2.4 Hysteresis loop.

Fig.2.5 Polarization mechanisms and their effect on the frequency dependence of the relative electric permittivity.

Fig.3.1 Powder form of NiO.

Fig.3.2 Powder form of CoO.

Fig.3.3 Powder form of ZnO.

Fig.3.4 Powder form of Fe_2O_3 .

Fig.3.5 Powder form of V_2O_5 .

Fig.3.6 A Balance.

Fig.3.7 Mortar and Pestle.

Fig.3.8 Typical diagram of a programmable electric furnace.

Fig.3.9 Schematic diagram of uniaxial pressing technique.

Fig.3.10 Typical diagram of a Hydraulic press.

Fig.3.11 Flow chart of the stages in preparation of spinel ferrite.

Fig.3.12 Sample Preparation in Solid State Reaction Method.

Fig.3.13 Polisher machine.

Fig.3.14. Toroid and Cylindrical shaped samples.

Fig.3.15 X-ray diffraction system.

Fig.3.16 A basic instrument for the Bragg spectrometer.

Fig.3.17 Geometry of the incident X-rays impinging the sample satisfying Bragg's law.

Fig. 3.18 Field Emission Scanning Electron Microscope (FESEM) setup.

Fig.3.19 A basic instrument for SEM.

Fig.3.20 A basic instrumental setup for EDX.

Fig3.21 Characteristic X-ray Generation Process.

Fig.3.22 Vibrating Sample Magnetometer.

Fig.3.23 A block diagram of PPMS setup.

Fig.3.24 Experimental setup of Wayne Kerr Impedance Analyzer (6500B).

Fig.3.25 Toroid shaped sample for the measurement of permeability.

Fig.3.26 (a) An impedance plot with the corresponding equivalent circuit and (b) Impedance plot an ideal polycrystalline sample with the equivalent circuit.

Fig.4.1 XRD patterns of $\text{Ni}_{0.62}\text{Co}_{0.03}\text{Zn}_{0.35}\text{Fe}_2\text{O}_4 + x\text{V}_2\text{O}_5$ sintered at 1200°C .

Fig.4.2 Variation of apparent lattice parameter, a (\AA) with $F(\theta)$ for V_2O_5 added Ni-Co-Zn ferrites having the compositions $\text{Ni}_{0.62}\text{Co}_{0.03}\text{Zn}_{0.35}\text{Fe}_2\text{O}_4 + x\text{V}_2\text{O}_5$, where a) $x=0.0\text{wt}\%$, b) $x=0.5\text{wt}\%$, c) $x=1.0\text{wt}\%$ and d) $x=1.5\text{wt}\%$.

Fig.4.3 Variation of the experimental lattice parameters 'a' with V_2O_5 (wt%) contents.

Fig.4.4 Variation of bulk density with V_2O_5 (wt%) contents.

Fig.4.5 Variation of X-ray density with V_2O_5 (wt%) contents.

Fig.4.6 Variation of % porosity with V_2O_5 (wt%) contents.

Fig.4.7 FESEM photomicrograph of $Ni_{0.62}Co_{0.03}Zn_{0.35}Fe_2O_4 + xV_2O_5$ sintered at $1200^\circ C$ where, (a) $x=0.0wt\%$, (b) $x=0.5wt\%$, (c) $x=1.0wt\%$ and (d) $x=1.5wt\%$.

Fig.4.8 EDX spectra of $Ni_{0.62}Co_{0.03}Zn_{0.35}Fe_2O_4 + xV_2O_5$, where (a) $x=0.0wt\%$, (b) $x=0.5wt\%$, (c) $x=1.0wt\%$ and (d) $x=1.5wt\%$ sintered at $1200^\circ C$.

Fig.4.9 The magnetization (M) with the applied magnetic field (H).

Fig.4.10 Variation of saturation magnetization, M_s , with V_2O_5 (wt%) contents.

Fig.4.11 The magnetization (M) versus the applied magnetic field (H) curves at different temperature for $Ni_{0.62}Co_{0.03}Zn_{0.35}Fe_2O_4 + xV_2O_5$, where a) $x=0.0wt\%$, b) $x=0.5wt\%$, c) $x=1.0wt\%$ and d) $x=1.5wt\%$ sintered at $1200^\circ C$.

Fig.4.12 Experimental magnetic moment at different temperatures.

Fig.4.13 Changes of Magnetization (M) and $\frac{dM}{dT}$ with temperature for a) $x=0.0wt\%$, b) $x=0.5wt\%$, (c) $x=1.0wt\%$ and (d) $x= 1.5wt\%$ V_2O_5 .

Fig.4.14 Variation of the real part of the initial permeability with frequency.

Fig.4.15 Variation of the imaginary part of the initial permeability with frequency.

Fig.4.16 Variation of Relative Quality factor (RFQ) with frequency.

Fig.4.17 Variation of Real part of dielectric with frequency.

Fig.4.25 Variation of Imaginary part of dielectric constant with frequency.

Fig.4.26 Variation of Loss factor as a function of frequency.

Fig.4.27 Variation of Resistivity with frequency.

Fig.4.28 Variation of (a) Z' and (b) Z'' , as a function of frequency.

List of Tables

Table 4.1 Crystallite size (t), Lattice parameter (a), X-ray density (ρ_x), Bulk density (ρ_B) and Porosity (P%) for the $\text{Ni}_{0.62}\text{Co}_{0.03}\text{Zn}_{0.35}\text{Fe}_2\text{O}_4 + x\text{V}_2\text{O}_5$ sintered at 1200°

Table 4.2 Average grain size, D of $\text{Ni}_{0.62}\text{Co}_{0.03}\text{Zn}_{0.35}\text{Fe}_2\text{O}_4 + x\text{V}_2\text{O}_5$ sintered at 1200°C .

Table 4.3 Data of EDX for $\text{Ni}_{0.62}\text{Co}_{0.03}\text{Zn}_{0.35}\text{Fe}_2\text{O}_4 + x\text{V}_2\text{O}_5$ spinel ferrites.

Table 4.4 Experimental magnetic moment for different compositions at 300K.

Table 4.5 Curie Temperature (T_c) for $\text{Ni}_{0.62}\text{Co}_{0.03}\text{Zn}_{0.35}\text{Fe}_2\text{O}_4 + x\text{V}_2\text{O}_5$ spinel ferrites.

LIST OF ABBREVIATION

AC	Alternating current
B	Magnetic induction
XRD	X-ray Diffraction
FESEM	Field Emission Scanning Electron Microscopy
$F(\theta)$	Nelson-Riley function
f_r	Resonance frequency
H_c	Critical field
J	Exchange integral
K	Total anisotropy
L_s	Self-inductance of the sample core
L_o	Inductance of the winding coil without sample
M	Magnetization
M_s	Saturation magnetization
N_A	Avogadro's number
P	Porosity
RQF	Relative Quality factor
T_c	Curie temperature
T_N	Neel temperature
T_s	Sintering temperature
Z	Complex impedance
EDS	Energy Dispersion Spectroscopy

CHAPTER 1 INTRODUCTION

1.1 Spinel Ferrites

Spinel ferrites are the class of ferrimagnetic materials which have significant role in electronic industries due to their different potential applications such as radar absorbers, antenna rod, inductors, loudspeakers, broadband transformers, high frequency transform, switching device and magnetic recording system[1-2]. Ferrites are magnetic materials which consist of double oxides of iron and another metal oxide. The general chemical formula of the ferrites is MFe_2O_4 , where M is denoted a divalent metal ion such as Fe^{2+} , Co^{2+} , Mn^{2+} , Ni^{2+} , Cu^{2+} , Zn^{2+} , Mg^{2+} or Cd^{2+} . There are different types of spinel ferrites: normal spinel and inverse spinel ferrites. Also, it can be written as general formula with $(M_xFe_{1-x})_A[M_{1-x}Fe_{1+x}]_BO_4$, where the first term within the first bracket indicates the tetrahedral or A sites and the second term within the square bracket indicates the octahedral B or sites [3]. (i) When $x = 1$, it is called normal spinel. In this type of ferrites, the divalent metal ions occupy in A-sites and the trivalent ions occupy in B-sites. $ZnFe_2O_4$ and $CdFe_2O_4$ are the examples of normal spinel ferrites. The cation distributions for $ZnFe_2O_4$ and $CdFe_2O_4$ are $(Zn)_A[Fe_2]_BO_4$ and $(Cd)_A[Fe_2]_BO_4$, respectively. (ii) When $x = 0$, it is called inverse spinel and $NiFe_2O_4$, $CoFe_2O_4$, $CuFe_2O_4$ are the inverse spinel ferrites. In inverse spinel ferrite, one trivalent Fe^{3+} is at the tetrahedral or A sites, while the remaining trivalent Fe^{3+} and the divalent metallic ions M^{2+} are at the B sites. The cation distributions for $CoFe_2O_4$ and $NiFe_2O_4$ are $(Fe)_A[CoFe]_B$ and $(Fe)_A[NiFe]_B$, respectively.

1.2 Motivation

Ni-Zn mixed ferrites are highly important ferrimagnetic materials which have widely used in electronic industries as well as communication technology due to their high magnetic permeability, high dielectric constant, low dielectric loss, higher resistivity, mechanical strength and chemical stability [4]. Ghodake *et al.* studied magnetic and microwave absorbing properties of Co^{2+} substituted Ni-Zn ferrites with the emphasis on

initial permeability [5]. Co substituted Ni-Zn ferrites having general chemical formula $Zn_{0.35}Ni_{0.60-x}Co_xFe_{2.05}O_4$ (where $x = 0.0, 0.10, 0.20$ and 0.40) were prepared by combustion method. It was found that saturation magnetization, coercivity and retentivity were increased with increasing of Co contents in Ni-Zn ferrites. They found that the reflection loss of sample $Zn_{0.35}Ni_{0.30}Co_{0.30}Fe_{2.05}O_4$ is higher than that of other compositions. Therefore Ni-Co-Zn ferrites can be employed in rubber composite microwave absorber as well as radar application. Raju *et al.* studied the effect of Zn substitution on the structural and magnetic properties of Ni-Co ferrites. They prepared a series of compositions of $Ni_{0.5}Co_{0.5-x}Zn_xFe_2O_4$ (0 to 0.5) by the citrate based sol-gel method. These samples have shown the cubic structure and lattice parameters increased due to increase of Zn contents. It was observed that the saturation magnetization was increased with Zn concentration up to $x=0.3$ and further decreased.

Additives have formed liquid phase during sintering process which is used as the sintering aids in the spinel ferrites. There are different additive such as V_2O_5 , MoO_3 , Bi_2O_3 , WO_3 and PbO which have been used in different spinel ferrites in order to improve the electromagnetic properties of the spinel ferrites [6]. Mirzaee *et al.* [7] observed the influence of V_2O_5 as an effective dopant on the microstructure development and magnetic properties of $Ni_{0.64}Zn_{0.36}Fe_2O_4$. V_2O_5 added $Ni_{0.64}Zn_{0.36}Fe_2O_4$ different compositions were prepared using standard solid state reaction method. They found that the permeability and relative density were increased with increasing the amount of V_2O_5 up to 1.6 wt%. Curie temperatures (T_c) were found to be maximum for 0.8wt% V_2O_5 content. It is increased by about 5% from $Ni_{0.64}Zn_{0.36}Fe_2O_4$ sample without addition of V_2O_5 . The average grain size was larger at 1.6wt% V_2O_5 in compare to other compositions. Janghorban *et al.* [8] studied the influence of V_2O_5 addition on the grain growth and magnetic properties of Mn-Zn high permeability ferrites. The Curie temperature was found to increase at 1.0wt% V_2O_5 which is $330^\circ C$ or $603K$. It was observed that the permeability of Mn-Zn ferrites were increased for small amount of additive V_2O_5 content ($< 0.03wt\%$), but it decreases for the higher amount of V_2O_5 wt% additive. Herrera *et al.* [9] studied the microstructure dependence of the magnetic properties of sintered Ni-Zn ferrites by solid-state reaction doped with V_2O_3 . They

focused in this work is to develop the high frequency range operation of $\text{Ni}_{0.7}\text{Zn}_{0.3}\text{Fe}_2\text{O}_4$ doped for 0.25, 0.50 and 0.75wt% V_2O_3 contents. The crystal phase of V_2O_3 added Ni-Zn ferrites showed a single cubic spinel structure. Due to the addition of V_2O_3 in $\text{Ni}_{0.7}\text{Zn}_{0.3}\text{Fe}_2\text{O}_4$ composition has been performed abnormal grain growth and the presence of porosity as a result the initial permeability, μ' and saturation magnetization, M_s have been decreased but the value of coercivity increased. This material will be good candidate as radar absorbing material in the microwave frequency range. Complex permeability spectra of Ni-Zn ferrites Co doped with $\text{V}_2\text{O}_5/\text{Nb}_2\text{O}_5$ was investigated by Rao *et al.* [10]. Co-doped Ni-Zn ferrites with different compositions were prepared by the conventional ceramic method. It was found that the microstructures of Nb_2O_5 added samples at lower concentration did not promote the grain growth for sintering temperature of 1250°C . Whereas the microstructure at higher concentration has been revealed larger grain growth. Also, vanadium doped in nickel-zinc ferrites has been shown high densities due to lower melting point of V_2O_5 . It was also found that the complex magnetic permeability spectra of these ferrites have constant frequency responses up to a few MHz. Kaiser *et al.* investigated the influence of V_2O_5 ion addition on the conductivity and grain growth of Ni-Zn-Cu ferrites [11]. It was found that $\text{Ni}_{0.6+x}\text{Zn}_{0.2}\text{Cu}_{0.2}\text{V}_x\text{Fe}_{2-2x}\text{O}_4$ (where $x = 0.0, 0.05, 0.10, 0.15, 0.20, 0.25$) was single phase cubic spinel structure. The bulk density, porosity and grain size were increased with the amount of V_2O_5 contents. Also, the semiconducting behavior and transition temperate have been decreased due to the light of electron hopping between Fe^{2+} and Fe^{3+} and a hole hopping between Ni^{3+} and Ni^{2+} with increasing V_2O_5 . The addition of V_2O_5 has been played a vital role to improve grain growth and domain size. As a result the ferrites materials were improved their magnetic and electrical properties by addition of sintering aids other than that of doping. There are a few research works on structural, magnetic and electrical properties of Ni-Co-Zn ferrites with the addition of V_2O_5 . V_2O_5 has liquid phase which play a role in order to improve the microstructure and magnetic properties of the spinel ferrites. Therefore, it is necessary to know the role of high valence ions (V^{5+}) in controlling the magnetic and electrical properties for the valuable applications in electromagnetic devices in our modern electronic industry. In the present thesis, a detailed study has been carried out to

examine the effect of V_2O_5 addition on structural, magnetic and electrical properties of Ni-Co-Zn ferrites.

1.3 Objectives of the present study .

The specific objectives of the present research are

- (i) Preparation of $Ni_{0.62}Co_{0.03}Zn_{0.35}Fe_2O_4 + xV_2O_5$ (where $x = 0.0, 0.5, 1.0,$ and $1.5wt\%$) compositions using standard solid state reaction method.
- (ii) Observation of the crystal structure of the prepared samples using X-ray diffraction (XRD) technique.
- (iii) Investigation of the surface morphology and compositional analyses using Scanning Electron Microscopy (SEM) and Energy Dispersive X-ray (EDX), respectively.
- (iv) Observation of the M-H curve at room temperature for the different compositions.
- (v) Study of Curie temperature (T_c) from M-T curve for all samples.
- (vi) Observation of the complex magnetic permeability as a function of frequency at room temperature for all samples.
- (vii) Measurement of the relative dielectric constant and dielectric loss as a function of frequency at room temperature.
- (viii) Investigation of the electrical resistivity as a function of frequency for all compositions.

1.4 Outline of the thesis

The organization of this thesis is as follows:

In **chapter-1**, deals with the importance of ferrites, spinel ferrites, literature review of research and objectives of the present work.

In **chapter-2**, gives literature review survey of earlier research, crystal structure of the spinel and theoretical backgrounds.

In **chapter-3**, gives the details of the sample preparation, describes the experimental part and descriptions of different measurement techniques that have been used in this research work.

In **chapter-4**, shows the results and discussion for various investigations in this research study.

In **chapter -5**, represents the conclusion of the overall experimental results.

CHAPTER 2 LITERATURE REVIEW AND THEORETICAL ASPECTS

2.1 Literature Review

Many researchers have studied on structural, surface morphology, magnetic and electrical properties of Ni-Zn ferrites for the applications in electronic and communication technology. These are discussed as follows:

The effect of Zn substitution on the structural and magnetic properties of Ni-Co ferrites having the formula $\text{Ni}_{0.5}\text{Co}_{0.5-x}\text{Zn}_x\text{Fe}_2\text{O}_4$ ($0 \leq x \leq 0.5$) were studied by Raju *et al.* [1]. The compositions were prepared by sol-gel method. They found that the saturation magnetization was increased with increasing of Zn content at the lower region. This could be attributed to the strongest super-exchange interaction between the sub-lattices in the spinel ferrite system. But the saturation magnetization decreases with the increase of Zn contents at the Zn-rich region, which is due to the effect of Yafet-Kittel. The strong magneto-crystalline anisotropy of Ni-Co-Zn ferrite comes from mainly Co^{2+} ions in the octahedral sites of spinel structure. The high coercive field is obtained due to spin-orbit coupling for the large anisotropy of cobalt ions. The substitution of Zn into the Co site leads to a decrease in the anisotropy.

Satyanarayan *et al.* [2] studied the structural, dielectric and magnetic properties of Al^{3+} and Cr^{3+} substituted Ni-Zn-Cu ferrites having the chemical formula $\text{Ni}_{0.7}\text{Zn}_{0.2}\text{Cu}_{0.1}\text{Fe}_{1.9}\text{M}_{0.1}\text{O}_4$ ($\text{M} = \text{Al}$ and Cr). The samples were prepared by solid state reaction method. They showed that the formation of the crystal structure was cubic spinel structure from X-ray diffraction method. They found the saturation magnetization, magnetic moment and coercive field for all samples from magnetic measurement (M-H curve). Al^{3+} substituted in Ni-Zn-Cu ferrites, the coercivity was decreased which leads to a soft magnetic material. The dc resistivity was measured and it is decreased with increasing of frequency. The complex magnetic permeability with

frequency was done from Wayne-Kerr network analyser at room temperature from 20 to 120 MHz. It was also found that the initial permeability was found to be increased for Cr substituted Ni-Zn-Cu ferrites in compare to Al substituted Ni-Zn-Cu ferrites.

Huang *et al.* [3] studied the microwave absorption mechanisms of the Ni-Zn ferrite nanofibers. They prepared $\text{Ni}_x\text{Zn}_{(1-x)}\text{Fe}_2\text{O}_4$ ($x = 0.2, 0.4, 0.5, 0.6, 0.8$) nanofibers with electro-spinning method. By tuning of the Ni^{2+} , they were developed the structural and magnetic properties of the samples. Finally, the excellent microwave absorption properties were performed with $\text{Ni}_{0.5}\text{Zn}_{0.5}\text{Fe}_2\text{O}_4$ nanofibers. The one dimensional Ni-Zn ferrites nanofibers have shown the efficient nanoscale microwave absorber and this property is very much significant for investigating of the microwave absorption mechanism in the spinel ferrites.

Ghodake *et al.* [5] observed the electric properties of Co substituted Ni-Zn ferrites. They prepared nano-crystalline Ni-Co-Zn ferrites using chemical co-precipitation method. The structural property was investigated by X-ray diffraction method and it was found the cubic phase structure of the samples. The electrical property, in particular, the electrical resistivity was found to increase with the doping of Co^{2+} content in the Ni-Zn ferrites matrix. The values of activation energy in paramagnetic region are found to be higher than that of ferrimagnetic region, which could be attributed to the magnetic ordering. The relative dielectric constant and dielectric loss tangent were decreased with the substitution of Co^{2+} contents in Ni-Zn ferrites.

An additive may play an important role in order to modify the electromagnetic properties of the spinel ferrite. There are different types of additive such as V_2O_5 , Nb_2O_3 , MoO_3 and Bi_2O_3 , which have been used as the suntrap aid in order to modify the electromagnetic properties. These are discussed as below:

Mirzaee *et al.* [7] observed the influence of V_2O_5 as an effective dopant on the microstructure development and magnetic properties of $\text{Ni}_{0.64}\text{Zn}_{0.36}\text{Fe}_2\text{O}_4$ soft ferrites. They prepared $\text{Ni}_{0.64}\text{Zn}_{0.36}\text{Fe}_2\text{O}_4$ composition by solid state

reaction. V_2O_5 was added with the studied ferrite in the range 0 to 3.2wt% in the steps of 0.4wt%. They have shown that the permeability, relative density and grain size were initially increased with increasing amount of V_2O_5 up to 1.6wt% and then decreased. The Curie temperature (T_c) was increased with additions of V_2O_5 up to 0.8wt% V_2O_5 and it was found to be $265^{\circ}C$.

Janghorban *et al.* [8] studied the influence of V_2O_5 addition on the grain growth and magnetic properties of Mn-Zn ferrites. The samples were prepared by solid state reaction method. This observation found that the permeability of Mn-Zn ferrites were increased for small amount of V_2O_5 additive (<0.03wt%), but it was decreased for the higher amounts of additive. The Curie temperature and saturation magnetization were increased by adding of V_2O_5 additive in a certain percentage and then it decreased. At low concentration 0.02wt% V_2O_5 , the magnetic permeability was increased by 42% than that of pure Mn-Zn ferrites.

Herrera *et al.* [9] studied the microstructure dependence of the magnetic properties of Ni-Zn ferrites by solid-state reaction doped with V_2O_3 . They focused in this work to develop the high frequency range operation of $Ni_{0.7}Zn_{0.3}Fe_2O_4$ ferrites. Ni-Zn ferrites were doped with V_2O_3 for different (0.25, 0.50 and 0.75wt %) concentrations. It showed a single cubic spinel phase crystal structure which was confirmed by an X-ray diffraction method. This working material can be used in radar absorbing material in the microwave frequency range.

Complex permeability spectra of Ni-Zn ferrites doped with V_2O_5/Nb_2O_5 was investigated by Rao *et al.* [10]. They prepared the samples with conventional ceramic method. The sample with V_2O_5 additive was sintered at $1210^{\circ}C$, whereas the sample with Nb_2O_5 was sintered at $1250^{\circ}C$. It was found that the microstructures of Nb_2O_5 added samples at lower concentration did not promote the grain growth for sintering temperature of $1250^{\circ}C$, while the microstructure at higher concentration reveals larger grain growth. On the other hand, the vanadium doped in Ni-Zn ferrites show high densities due to lower melting point of V_2O_5 . It was also found that the complex magnetic

permeability spectra of these ferrites have constant frequency responses up to a few MHz. The permeability spectra can be explained as the combined effect of the spin relaxation and domain walls.

Ghodake *et al.* [12] studied magnetic and microwave absorbing properties of Co^{2+} substituted Ni-Zn ferrites with the emphasis on initial permeability. Ferrite samples with the general formula $\text{Zn}_{0.35}\text{Ni}_{0.60-x}\text{Co}_x\text{Fe}_{2.05}\text{O}_4$ (where $x=0.0, 0.1, 0.2$ and 0.4) were prepared by combustion method. They observed the crystal structure with cubic phase spinel structure. It was found that saturation magnetization of Co substituted Ni-Zn ferrite is higher than that of pure Ni-Zn ferrites. In complex permeability measurement, the real part of initial permeability was almost independent with frequency and it increases with Co contents. It was found that the reflection loss of sample $\text{Zn}_{0.35}\text{Ni}_{0.30}\text{Co}_{0.3}\text{Fe}_{2.05}\text{O}_4$ is higher than that of other samples. Therefore, it can be used in rubber composite microwave absorber as well as radar application.

Patil *et al.* [13] studied the effect of V_2O_5 addition on electrical and dielectric properties of Ni-Zn ferrite. They prepared the samples having the formula $\text{Ni}_{0.7}\text{Zn}_{0.3}\text{Fe}_2\text{O}_4 + x\text{V}_2\text{O}_5$ (where $x=0.0$ and 0.2) using standard solid state reaction method. It was found that the activation energy in paramagnetic region is higher than that of ferrimagnetic region. The resistivity of V^{5+} substituted Ni-Zn ferrites is higher than that of pure spinel ferrite at room temperature. On the other hand, the relative dielectric constant and loss tangent were decreased at higher V^{5+} contents. The obtained parameters can be used in high frequency magnetic devices.

Lebourgeois *et al.* [14] observed the influence of V_2O_5 on the magnetic properties of Ni-Zn-Cu ferrites. The ferrite samples have been prepared with solid state reaction. It was observed that the magnetic properties were deteriorated for the content higher than that of 0.6wt% V_2O_5 . The micro structural property can be improved with the tuning of the sintering range. The complex permeability of ferrite samples with toroid shaped was measured by impedance analyzer from 1MHz to 1.8GHz. The magnetic permeability was decreased due to the various defects in the grain. These

defect come from the domain walls and pores in the sample and then decline to permeability.

Influence of MoO_3 and V_2O_5 co-doping on the magnetic properties and microstructures of Ni-Zn ferrite were observed by Mirzaee *et al.* [15]. The ferrites have been prepared by conventional powder method. In this study, they were used Fe_2O_3 , ZnO, NiO, V_2O_5 and MoO_3 as the raw materials to prepare of ferrites. The compositions were sintered at different temperatures. It was found that the samples doped with V_2O_5 and MoO_3 have shown lower power loss in compare to pure Ni-Zn spinel ferrites.

2.2 Theoretical Aspects

2.2.1 Magnetism in Solids

When a solid is placed in a magnetic field, it gets magnetized. The magnetic moment per unit volume developed inside a solid is called magnetization and is denoted by M . The magnetic susceptibility, χ , which is the measure of the quality of the magnetic material and it's defined as the magnetization produced per unit applied magnetic field.

$$\chi = \frac{M}{H} \quad (2.1)$$

where \mathbf{H} is the strength of the applied magnetic field. As the vectors \mathbf{M} and \mathbf{H} can, in general, have different direction, χ is a tensor. However, in isotropic media, \mathbf{M} and \mathbf{H} are in the same direction and χ is the scalar quantity. The magnetic induction or magnetic flux density \mathbf{B} produced inside the medium as a consequence of the applied magnetic field \mathbf{H} and is given by

$$\mathbf{B} = \mu_0(\mathbf{H} + \mathbf{M}) \quad (2.2)$$

where μ_0 is the permeability of the free space or vacuum and equal to $4\pi \times 10^{-7} \text{ Hm}^{-1}$. The unit of \mathbf{B} is Wbm^{-2} or Tesla (T). From equations (2.1) and (2.2)

$$\mathbf{B} = \mu_0(1 + \chi)\mathbf{H} \quad (2.3)$$

$$\mathbf{B} = \mu\mathbf{H} \quad (2.4)$$

Where, μ is called the absolute permeability of the medium. It is more convenient to introduce a dimensionless parameter μ_r which is called the relative permeability of the medium and is given by

$$\mu_r = \frac{\mu}{\mu_0}$$

Or, $\mu = \mu_0\mu_r \quad (2.5)$

Thus, Equation (2.4) becomes

$$\mathbf{B} = \mu_0\mu_r\mathbf{H} \quad (2.6)$$

Combining equation (2.3) with equation (2.6),

$$\mu_r = 1 + \chi \quad (2.7)$$

In the absence of any materials medium, $\mathbf{M} = 0$, $\chi = 0$, $\mu = \mu_0$ and $\mu_r = 1$, and from above relations, then obtain

$$\mathbf{B} = \mu_0\mathbf{H} \quad (2.8)$$

According to the modern theories, the magnetism in solids arises due to orbital and spins motions of electrons as well as spins of the nuclei. The motion of electrons is equivalent to an electric current which produces the magnetic effects. The major contribution comes from the spin of unpaired valence electrons which produces permanent electronic magnetic moments. Thus the nature of magnetization produced depends on the number of

unpaired valence electrons present in the atoms of the solid and on the relative orientations of the neighboring magnetic moments.

2.2.2 Magnetic ordering

The onset of magnetic order in solids has two basic requirements:

- i) Individual atoms should have magnetic moments (spins)
- ii) Exchange interactions should exist in between them.

Magnetic moments are originated in solids as the consequence of overlapping of the electronic wave functions with those of neighboring atoms. This condition is best fulfilled by some transition metals and rare-earths. The exchange interactions depend sensitively upon the interatomic distance and the nature of the chemical bonds, particularly of nearest neighbor atoms. When the positive exchange dominates, which corresponds to parallel coupling of neighboring atomic moments (spins), the magnetic system becomes ferromagnetic below a certain temperature, T_c called the Curie temperature. The spin directions are determined by the minimum of magneto-crystalline anisotropy energy of the crystal. Therefore, ferromagnetic substances are characterized by spontaneous magnetization. But a ferromagnetic material in the demagnetized state displays no net magnetization in zero field because in the demagnetized state a ferromagnetic of macroscopic size is divided into a number of small regions called domains, spontaneously magnetized to saturation value and the directions of these spontaneous magnetization of the various domains are such that the net magnetization of the specimen is zero. The existence of domains is a consequence of energy minimization. The size and formation of these domains are in a complicated manner dependent on the shape of the specimen as well as its magnetic and thermal history. When negative exchange dominates, adjacent atomic moments (spins) align anti-parallel to each other, and the substance is said to be anti-ferromagnetic below a characteristic temperature, T_N , called the Neel temperature. In the simplest case, the lattice

of an antiferromagnetic is divided into two sub lattices with the magnetic moments of these in anti-parallel alignment.

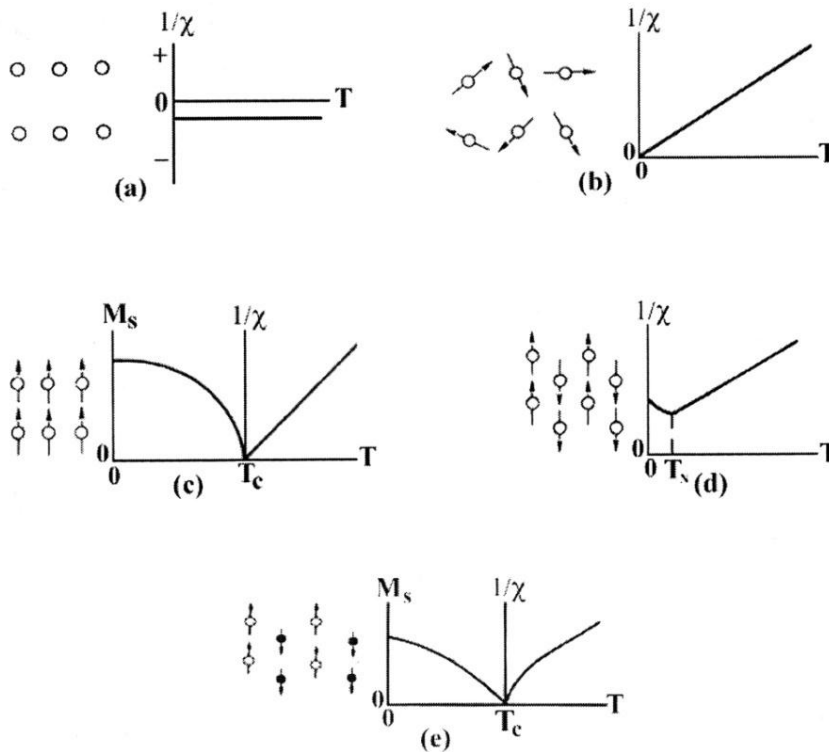


Fig.2.1 Temperature dependence of the inverse susceptibility for:(a) a diamagnetic material; (b) a paramagnetic material, showing Curie's law behavior; (c) a ferromagnetic material, showing a spontaneous magnetization for $T < T_c$ and Curie – Weiss behavior for $T > T_c$ (d) anti-ferromagnetic material; and (e) a ferrimagnetic material, showing a net spontaneous magnetization for $T < T_c$ and non-linear behavior for $T > T_c$.

In ferrimagnetism there are also two sub-lattices with magnetic moments in opposite directions, but the magnetization of the sub-lattices are of unequal strength resulting in a non-zero magnetization and therefore has net spontaneous magnetization. At the macroscopic level of domain structures, ferromagnetic and ferrimagnetic materials are therefore similar. The Curie

and Neel temperatures are characterized a phase transition between the magnetically ordered and disordered states. A useful property for characterizing the magnetic materials is the magnetic susceptibility and defined as the magnetization, M , divided by the applied magnetic field, H i.e. $\chi = M/H$. The temperature dependence of susceptibility or, inverse of susceptibility is a good characterization parameter for magnetic materials. Fig.2.2 (a) shown the diamagnetic state of the materials in here the spin magnetic moment are randomly alien and net resultant magnetic moment zero, (b) shown the paramagnetic state of material in here the spin magnetic moments are randomly alien but the show a net magnetic moment with and external magnetic field applied, (c) shown the ferromagnetic state where the magnetic moment are spontaneous alien, (d) show the antiferrimagnetic state where the spin moment are equal and opposite direction and (e) shown the ferrite state where the spin moment are equal and opposite but their magnitude are not equal.

2.2.3 Ferrites

Ferrites have the cubic structure, which is very close to mineral spinel $MgO.Al_2O_3$ and are called cubic spinel. Analogous to the mineral spinel, magnetic spinel have the general formula, $MeO.Fe_2O_3$ or $MeFe_2O_4$, where Me is the divalent metal ion [16]. The structure was first determined by Bragg and Nishikawa [17-18]. Formerly, spinels containing Fe were called ferrites, but now the term has been broadened to include many other ferrimagnets including garnets and hexagonal ferrites and these need not necessarily contain iron. In the ideal spinel structure the anions form cubic close packing, in which the cations partly occupy the tetrahedral (A-sites) and octahedral (B-sites) interstices.

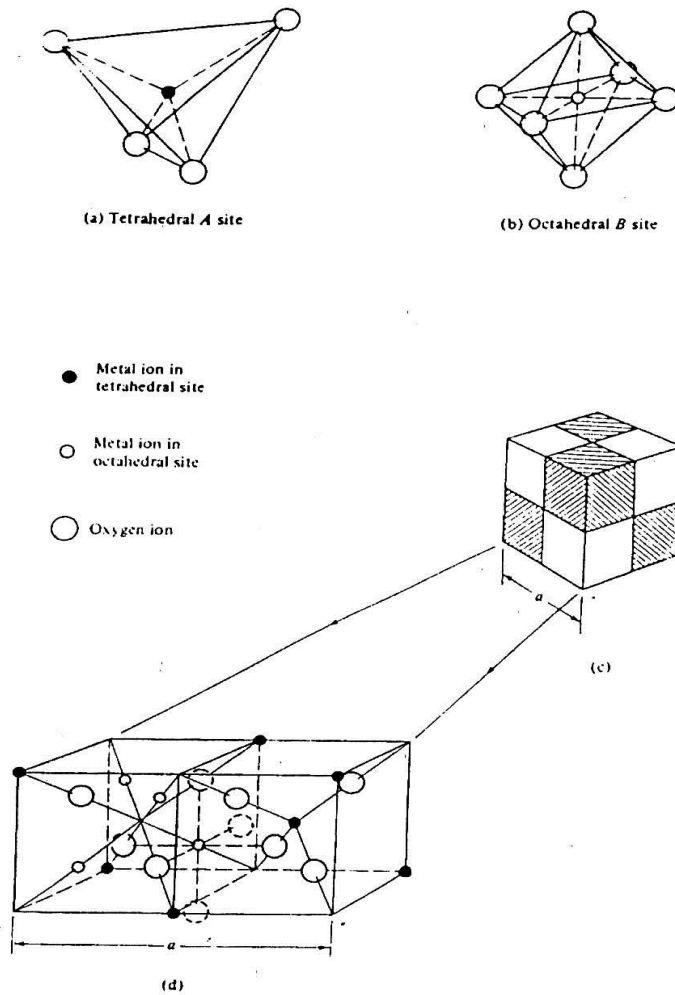


Fig.2.2 Unit cell of Cubic ferrite.

Now, the interstices are not all the same: some which we call A-sites are surrounded by or coordinated with 4 nearest neighboring oxygen ions whose lines connecting their centers form a tetrahedron. Thus, A-sites are called tetrahedral sites. The other types of B-sites are coordinated by 6 neighboring oxygen ions whose lines connecting their centers form an octahedron. Thus B-sites are called octahedral sites. In the unit cell of 32 oxygen ions there are 64 tetrahedral sites and 32 octahedral sites. It turns out that of the 64 tetrahedral sites, only 8 are occupied and out of 32 octahedral sites, only 16 are occupied. Thus structure of spinel compounds is complex; the unit cell contains 8 formula units AB_2O_4 , with 8 A-sites, 16 B-sites and 32 oxygen

ions, and total of $8 \times 7 = 56$ ions. A spinel unit cell contains two types of sub cells, the two types of sub cells alternate in a three dimensional array so that each fully repeating unit cell requires 8 sub cells. The positions of the ions in the spinel lattice are not perfectly regular and some distortion does occur. The tetrahedral sites are often too small for the metal ions so that the oxygen ions move slightly to accommodate them. The oxygen ions connected with the octahedral sites move in such a way as to shrink the size the octahedral cell by the same amount as the tetrahedral site expands. The movement of the tetrahedral oxygen is reflected in a quantity called the oxygen parameter, which is the distance between the oxygen ion and the face of the cube edge along the cube diagonal of the spinel sub-cell. This distance is theoretically equal to $3/8a_0$, where a_0 is the lattice constant. In spinel structure the distribution of cations over the tetrahedral or A sites and octahedral or B sites can be present in a variety of ways. If all the Me^{2+} ions in $Me^{2+} Me_2^{3+} O_4$ are in tetrahedral and all Me^{3+} ions in octahedral positions, the spinel is then called normal spinel. Another cation distribution in spinel exists, where one half of the cations Me^{3+} are in the A-sites and the rest, together with the Me^{2+} ions are randomly distributed among the B-sites.

The spinel having the latter kind of cation distribution is known as inverse spinel [19].

i) Normal Spinel: divalent metal ions are on A sites: $Me^{2+} [Me_2^{3+}] O_4$

ii) Inverse Spinel: divalent metal ions are on B sites: $Me^{3+} [Me^{2+} Me_2^{3+}] O_4$

A completely normal or inverse spinel represents the extreme cases; Zn-ferrites have normal spinel structure. On the other hand, Cu-ferrites have inverse spinel structure. There are many spinel oxides which have cation distributions intermediate between these two extreme cases and are called mixed spinel. The general cation distribution for the spinel can be written as: $(Me_x^{2+} Me_{1-x}^{3+}) [Me_{1-x}^{2+} Me_{1+x}^{3+}] O_4^{2-}$ where the first and third brackets represent the A and B sites, respectively.

2.2.4 Exchange Interaction in the spinel Ferrites.

Spontaneous magnetization of spinel ferrites can be obtained on the basis of their composition, cation distribution and the relative strength of the possible interaction. The super exchange interaction of the spinel ferrites are strongly depended on the tetrahedral (A) and octahedral (B) sites. The strongest super exchange interaction is expected to occur between octahedral and tetrahedral cations. The strength of interaction or exchange force between the moments of the two metals ions on different sites depends (i) on the distances between these ions and the oxygen ion that links them and (ii) on the angle between the three ions. The interaction is greatest for an angle of 180° where the interionic distances are the shortest.

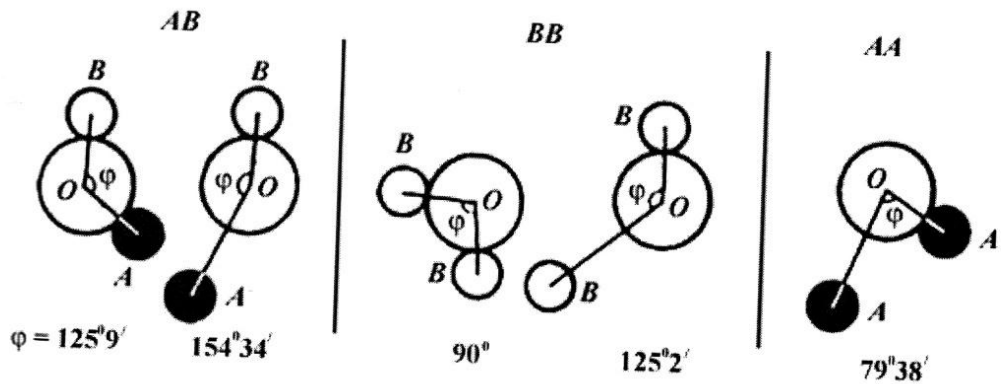


Fig.2.3 Inter ionic angles for the different type of lattice site interactions.

In the A-A and B-B cases, the angles are too small or the distances between the metal ions and the oxygen ions are too large. The best combination of distances and angles are seen in A-B interactions. For an undistorted spinel, the A-O-B angles are about 125° and 154° . The B-O-B angles are 90° and 125° but the latter, one of the B-B distances is large. In the A-A case the angle is about 80° . Therefore, the interaction between A and B sites is strongest. The B-B interaction is much weaker and the most unfavorable

situation occurs in the A-A interaction. The super-exchange cationic interactions are denoted by J_{AB} , J_{AA} and J_{BB} which are modified by introducing cationic substitutes with different valence states, radii or magnetic moments in either or both of the A and B sub-lattices [20].

2.2.5 The Two Sub-lattice Model

Consider two sub-lattice arrays A and B. Assume that an anti-ferromagnetic AB interaction, there are also anti-ferromagnetic interactions AA and BB [21].

Let the molecular fields at A and B are H_{ma} and H_{mb} . Then

$$H_{ma} = H - \alpha M_a - \beta M_b \quad (2.9)$$

$$H_{mb} = H - \beta M_a - \alpha M_b \quad (2.10)$$

where H is the applied field, M_a and M_b represent the magnetizations of A and B and α is the interaction parameter for two atoms having like spins (AA or BB) and β is the interaction parameter for two unlike atoms.

Now we consider two temperature regions:

when $T > T_N$ i.e. when temperature is above Neel temperature, we are far away from saturation and magnetization of lattice A is given by,

$$M_a = \left(\frac{N \mu^2}{3kT} \right) \cdot H_a \quad (2.11)$$

where $\mu^2 = \mu_B^2 g^2 J(J + 1)$ and N is the number of atoms per unit volume.

If we assume that dipoles on B site are identical with those on A site and there are equal number of A and B sites, then we have similarly,

$$M_b = \left(\frac{N \mu^2}{3kT} \right) \cdot H_b$$

$$M = M_a + M_b = \frac{N \mu^2}{3kT} [2H - (\alpha + \beta)M]$$

$$\text{or, } M \left[1 + \frac{N \mu^2}{3kT} (\alpha + \beta) \right] = \frac{2N \mu^2}{3kT} \cdot H$$

$$\text{or, } \chi = \frac{M}{H} = \frac{\frac{2N \mu^2}{3k}}{T + \frac{N \mu^2 (\alpha + \beta)}{3k}}$$

$$\text{or, } \chi = \frac{C}{T + \theta} \quad (2.12)$$

Comparing this expression with expression

$$\chi = \frac{M}{H} = \frac{C}{T - \theta}$$

For the susceptibility of a ferromagnetic above Curie temperature, it is quite obvious that an antiferromagnetic contains $T + \theta$. Further the Curie constant C is twice the Curie constant for individual A or B lattice. When $T < T_N$, At the Neel temperature T_N itself, we are still sufficiently far away from saturation effects.

We have,

$$M_a = -\frac{N\mu^2}{3kT_N}(\alpha M_a + \beta M_b)$$

$$\text{or } \left[1 + \frac{N\mu^2}{3kT_N} \cdot \alpha\right] M_a + \frac{N\mu^2}{3kT_N} \beta M_b = 0 \quad (2.13)$$

$$\text{Similarly, } \frac{N\mu^2}{3kT_N} \cdot \beta M_a + \left[1 + \frac{N\mu^2}{3kT_N} \cdot \alpha\right] M_b = 0 \quad (2.14)$$

These equations have a non-vanishing solution for M_a and M_b only if the determinant of their coefficient vanishes.

$$\text{Since, } C = \frac{N\mu^2}{3k} \text{ or } \begin{vmatrix} \left(1 + \frac{c}{2T_N} \cdot \alpha\right) & \frac{c}{2T_N} \cdot \beta \\ \frac{c}{2T_N} \cdot \beta & \left(1 + \frac{c}{2T_N} \cdot \alpha\right) \end{vmatrix} = 0$$

$$\text{or } \left[1 + \frac{c}{2T_N} \cdot \alpha\right]^2 - \frac{c^2}{4T_N^2} \cdot \beta^2 = 0$$

$$\text{or } 1 + \frac{c^2}{4T_N^2} \cdot \alpha^2 + \frac{c}{T_N} \alpha - \frac{c^2}{4T_N^2} \cdot \beta^2 = 0$$

$$\text{or } T_N^2 + \frac{c^2}{4} \cdot \alpha^2 + c\alpha \cdot T_N - \frac{c^2}{4} \beta^2 = 0$$

$$\text{or } T_N^2 + c\alpha \cdot T_N + \frac{c^2}{4} (\alpha^2 - \beta^2) = 0$$

$$\text{or } T_N = \frac{-c\alpha \pm \sqrt{\{c^2\alpha^2 - c^2(\alpha^2 - \beta^2)\}}}{2}$$

$$\text{or } T_N = \frac{c(\beta - \alpha)}{2}$$

From this expression it is quite obvious that Neel temperature increases as AB interaction (β) is stronger, where it decreases with AA or BB interaction (α) increasing. In this model the Neel temperature is not identical with θ . Setting up a relation between T_N and θ with the help of equation (4), we get,

$$\theta = \frac{N\mu^2}{3k} (\alpha + \beta) = \frac{C(\alpha+\beta)}{2}$$

Therefore,

$$\frac{T_N}{\theta} = \frac{(\beta-\alpha)}{(\beta+\alpha)} \quad (2.15)$$

It is to be noted that $T_N < 0$ indicates that it must be positive. Let us now consider the susceptibility of an antiferromagnetic material below Neel temperature. For simplicity we shall assume only AB interaction i.e., we shall assume, $\alpha = 0$. We consider two cases on two sub-lattice model, first, with the applied magnetic field perpendicular to the axis of spins and second, with the field parallel to the axis of spins.

Case I:

For the calculation of susceptibility, equilibrium is determined by the balance of an external force and a restoring force. In this case, field tends to line up the dipoles along the fields, but as a result of tendency for A and B to remain antiparallel, a compromise is obtained in which the dipoles make a certain angle, φ with original spin direction. In equilibrium, the resultant forces should lie along the line joining the two poles. So that for small angles we have

$$2\beta M_a \varphi = H$$

Which is opposite in direction of H, since $M_a = M_b$

The total magnetization along the external field direction is,

$$M = (M_a + M_b) = \frac{H}{\beta}$$

$$\chi_{\perp} = \frac{M}{H} = \frac{1}{\beta}$$

Thus χ_{\perp} is independent of temperature.

Case II:

The calculation of χ_{\perp} corresponding to an applied field along the axis of spins is complicated. It is given the susceptibility at $T=0\text{K}$ is zero, $\chi_{\perp} = 0$.

2.2.6 Hysteresis loop

The state of magnetization of a solid is a function of the strength and direction of the magnetizing field. If we consider a ferromagnetic material which contains many small magnetic domains but no net magnetization, we can examine what happens to the domains as the field strength is increased. As the field is increased from zero, the effect on the solid is to displace domain boundaries in a reversible fashion. If the magnetic field is switched off, the domain boundaries return to their starting positions. Thus the initial part of the B-H curve results from reversible domain boundary displacement and the slope is called initial permeability μ_i . As the magnetic field strength is increased there is an irreversible boundary displacement and at first the induced magnetization increases more rapidly and gives a maximum slope μ_{\max} . Finally in the upper part of the magnetization curve all domain boundaries have been displaced and further increase in the magnetic field cause rotation of the domains in the direction of the applied field. At this point the material is saturate, higher fields cannot induce more magnetization. As the magnetic field is decreased to zero, the induced magnetization does not decrease to zero but the alignment of most of the domains during magnetization results in a remanent magnetization or remanence B_r . When the direction of the magnetic field is reversed the induced magnetization decreases and finally becomes zero at a value of the magnetic field strength called the coercive force H_C . Further increased magnetic field strength in this opposite direction eventually causes magnetic saturation in the reverse direction and produces a saturation B_S and remanence B_r values of the same magnitude as in the first quadrant. As an applied field is cycled from one direction to the other direction, the Hysteresis loop is followed. Since the area

of the Hysteresis loop represents the energy or work to bring about changes in the magnetic domain structure, the product BH , called the energy product, represents a net loss in the system, usually in the form of heat. A material with a low coercivity is said to be soft and may be used in microwave devices, magnetic shielding, transformers or recording heads. Magnetic materials with high coercivity are called hard and are used to make permanent magnets. Permanent magnets find application in electric motors and magnetic recording media.

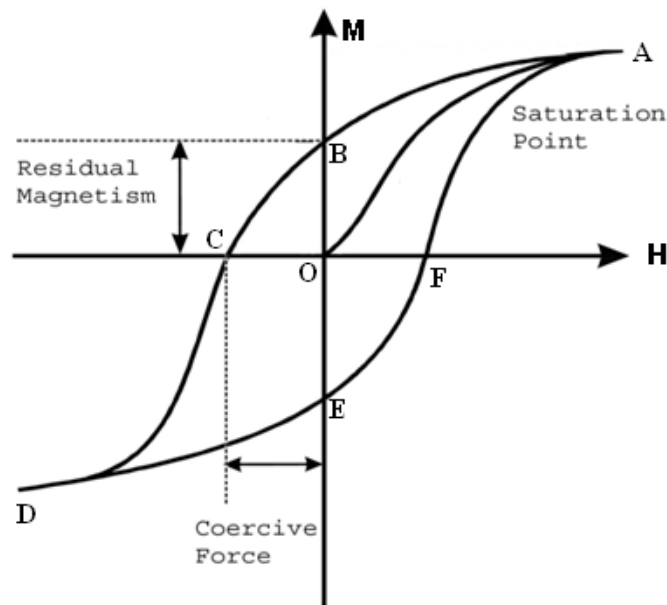


Fig.2.4 Hysteresis loop.

2.2.7 Maxwell-Wagner Polarization

The dielectric constant, ϵ of a material, is a term that refers to the material's ability to concentrate an electric field. As an example, the higher the dielectric constant of an insulator, the higher the capacitance it can provide when placed between two conducting plates, or in other words, it can store more charge for the same thickness of insulator. The dielectric constant

is related to how much a material can be polarized. When placed in an electric field, the atoms, molecules, or ions of a dielectric, respond to the applied electric field (E). It is actually the charges in the dielectric's atoms, molecules, or ions that will reorient themselves in the direction of the applied field. The more responsive are these charges belong to the higher the electric permittivity, ϵ of the dielectric. Since polarization is the "alignment of permanent or induced atomic or molecular dipole moments with an externally applied electric field" [22]. Several sources of polarization exist: space charge, electronics, ionic, and orientation polarization. Typically, dielectric materials exhibit at least one of these polarization mechanisms depending on the material and the manner of the external field frequency as shown in fig2.5.

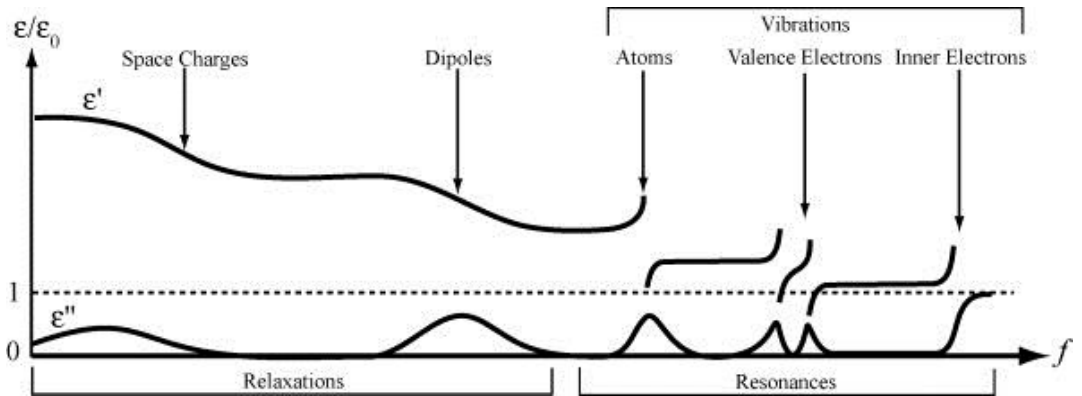


Fig.2.5 Polarization mechanisms and their effect on the frequency dependence of the relative electric permittivity.

The total polarization of a dielectric is consequently equal to the sum of all the polarization mechanisms in the material such as, space charge (P_s), electronic (P_e), ionic (P_{ion}) and orientation (P_0) polarizations.

$$P_{tot} = P_s + P_e + P_{ion} + P_0 \quad (2.16)$$

However, the space charges polarization is the so-called Maxwell-Wagner polarization. The electronic, the ionic and the dipole orientation polarization mechanisms have in common that they are caused by the displacement or orientation of bound charge carriers. These carriers are under the influence of the local field which depends on the total applied field and the polarization of the surroundings. However, the space-charge or interfacial polarization mechanism is produced by traveling charge carriers. Thus, the piling up of space-charge in a volume, or of surface charges at an interface, incorporates large-scale field patterns and as such it greatly affects the overall polarisability of a material/structure.

CHAPTER 3 SAMPLES PREPARATION AND CHARACTERIZATIONS

3.1 Samples Preparation

3.1.1 Raw Materials

Nickel (II) oxide is the chemical compound with the formula NiO. It is notable as being the well-characterized oxide of nickel [23]. It is classified as a basic metal oxide. There are some physical parameters of NiO as below:

- (i) Molecular mass is, $M = 74.6928$ g/mol.
- (ii) Density is, $\rho = 6.67$ g/cc.
- (iii) Melting point is, $T_m = 1955^\circ\text{C}$.
- (iv) Crystal structure is Cubic.
- (v) Lattice Constant, $a = 417.69$ pm.



Fig. 3.1 Powder form of NiO.

Cobalt (II) Oxide or Cobalt monoxide is an inorganic compound. It is an Olive-green or black powder. It is used extensively in the ceramic industries as an additive to create blue colored glazes and to produce Cobalt (II) salt [24]. There are some physical parameters of CoO as below:

- (i) Molecular mass is, $M = 74.9326 \text{ g/mol}$.
- (ii) Density is, $\rho = 6.44 \text{ g/cc}$.
- (iii) Melting point is, $T_m = 895^\circ\text{C}$ and Boiling point is, $T_b = 900^\circ\text{C}$.
- (iv) Crystal structure is Cubic.
- (v) Lattice Constant, $a = 426 \text{ pm}$.



Fig. 3.2 Powder form of CoO.

Zinc Oxide is an inorganic compound with the formula ZnO. ZnO is a white powder that is insoluble in water and it is widely used as an additive in numerous materials and products including rubbers, plastics, ceramics, glass, cement, ointment, foods, batteries, and ferrites [25]. There are some physical parameters as below:

- (i) Molecular mass is, $M = 81.406 \text{ g/mol}$.
- (ii) Density is, $\rho = 5.1 \text{ g/cc}$.
- (iii) Melting point is $T_m = 1974^\circ\text{C}$ and Boiling point is $T_b = 1974^\circ\text{C}$.
- (iv) Crystal structure is Wurtzite.
- (v) Lattice Constant, $a = 324.95 \text{ pm}$, $c = 520.69 \text{ pm}$.

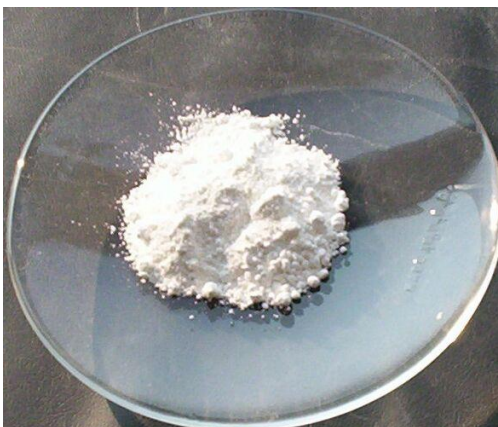


Fig. 3 .3 Powder form of ZnO.

Iron (III) oxide or ferric oxide is the inorganic compound with formula Fe_2O_3 . It is a red-brown solid [26]. Fe_2O_3 is the main source of iron for the steel industry. There are some physical parameters as following:

- (i) Molecular mass is, $M = 159.687 \text{ g/mol}$.
- (ii) Density is, $\rho = 5.25 \text{ g/cc}$.
- (iii) Melting point is, $T_m = 1539^\circ\text{C}$.
- (iv) Crystal structure is Rhombohedra.
- (v) Lattice Constant, $a = 917\text{pm}$, $b = 930\text{pm}$, $c = 850\text{pm}$.



Fig.3.4 Powder form of Fe_2O_3 .

Vanadium pentoxide (V_2O_5) is the inorganic compound. It is a brown or yellow solid. It is widely used in industrial catalyst [27]. There are few physical parameters as flowing:

- (i) Molecular mass is $M = 181.88$ g/mol.
- (ii) Density is, $\rho = 3.357$ g/cc.
- (iii) Melting point is, $T_m = 690^\circ\text{C}$ and Boiling point is, $T_b = 1750^\circ\text{C}$.
- (iv) Crystal structure is Orthorhombic.
- (v) Lattice Constant, $a=1151$ pm, $b=355.9$ pm, $c=437.1$ pm.



Fig. 3.5 Powder form of V_2O_5 .

3.1.2 Solid State Reaction Method

A goal common to all the ferrites is the common formation of the spinel structure. Now a days, Solid State Reaction technique or conventional ceramic process is easier and low cost method. So, major of the ferrite samples are made by the conventional ceramic process or Solid State Reaction technique. Most non-conventional process involves producing the powder by wet method. Among these methods, some are: (i) Co-precipitation, (ii) Organic Precursors, (iii) Sol-gel synthesis, (iv) Spray-drying (v) Freez-

drying, (vi) Combustion synthesis, (vii) Glass crystallization. Both the mechanical and chemical methods have some advantages and disadvantages. The advantages of the mechanical methods include large-scale production of bulk ceramic powder at low cost and comparatively easy adaptability [28].



Fig. 3.6 A Balance.

Chemical methods are generally used to prepare fine powder with improved homogeneity and densification. It is also easy to control the stoichiometry and particle size with less processing time. However, the chemical techniques are generally complex than the conventional solid state reaction and the large-scale production is sometimes difficult. In this research work, the most economical and comparatively simple mixed oxide process (conventional solid-state reaction technique) is used for preparing the different compositions of V_2O_5 added Ni-Co-Zn spinel ferrites. In the solid state reaction method, the required composition is usually started form the appropriate amount of raw mineral oxides or carbonates by crushing, grinding and milling. In this research work, the raw mineral oxides are mixed by hand milling in a mortar and pestle and it is in fig. 3.7.

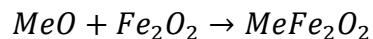
Milling can be carried out to increase the degree of mixing. This method depends on the solid state inter-diffusion between the raw materials. Solids do not usually react at room temperature for normal time scales.



Fig. 3.7 Mortar and Pestle.

Thus it is necessary to heat at high temperatures for the diffusion length $(2Dt)^{1/2}$ to exceed the particle size, where D is the diffusion constant for the fast diffusing species, and t is the firing time. The ground powders can then be calcined in air or oxygen at temperatures above 800°C . For some time, this process is continued until the mixture is converted into the correct crystalline phase. The calcined powders are again crushed into the correct crystalline phase. The pellets or toroid shaped samples are prepared from these calcined powders using die-punch assembly or hydrostatic or isostatic pressure. Sintering is carried out in the solid state, at temperatures ranging from 1100 – 1400°C , for times of typically 1–40 hours and in various atmospheres (e.g. Air, O_2 and N_2) [29–30]. Fig.3.11 shows, diagrammatically, the stages followed in ferrite preparation. During the calcining stage, the reaction of Fe_2O_3 with metal oxide (say, MeO or Me_2O_3) and adding some Me_2O_3 or Me_2O_5 takes place in the solid state to form spinel according to the reaction [31]:

The general solid state reaction leading to a ferrite MeFe_2O_4 may be represented as



Where Me is the divalent ion.



Fig.3.8 Typical diagram of a programmable electric furnace.

There are basically four steps in the preparation of ferrite:

1. Preparation of materials to form an intimate mixture with the metal ions in the ratio which they will have in the final product.
2. Heating of this mixture to form the ferrite (often called calcining).
3. Grinding the calcined powders and pressing the fine powders into the required shape and
4. Sintering to produce a highly densified product.

3.1.3 Calcining, Pressing and Sintering

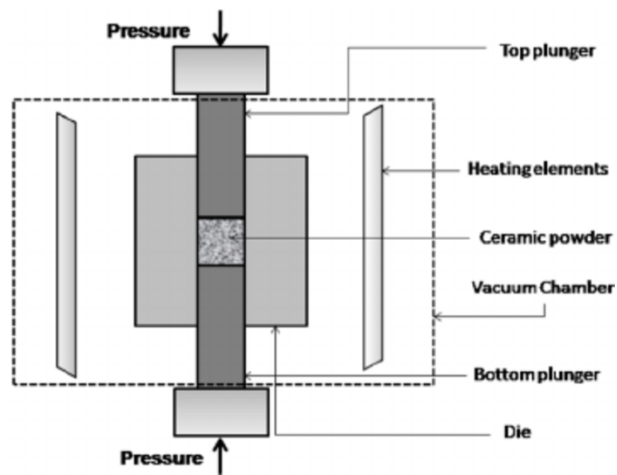
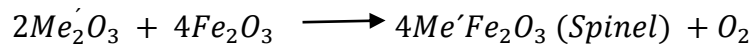


Fig. 3.9 Schematic diagram of uniaxial pressing technique.

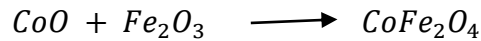
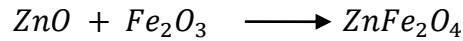
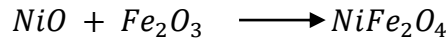
Calcining is defined as the process of obtaining a homogeneous and phase pure composition of mixed powders by heating them for a certain time at a high temperature and then allowing it to cool slowly.



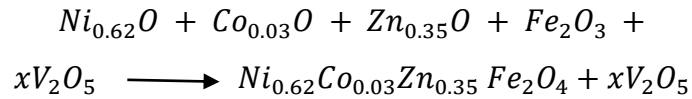
Fig. 3.10 Typical diagram of a Hydraulic press.



The NiO, CoO, ZnO are creeps into Fe_2O_3 as given bellow, to form an intermediate phase



After the V_2O_5 is added



The calcining process can be repeated several times to obtain a high degree of homogeneity. The calcined powders are crushed into fine powders. The ideal characteristics of fine powders are [32]:

1. Small particle size (sub-micron).
2. Narrow distribution in particle size.
3. Dispersed particles.
4. Equiaxed shape of particle.
5. High purity.
6. Homogeneous composition.

A small particle size of the reactant powders provides a high contact surface area for initiation of the solid state reaction; diffusion paths are shorted, leading to more efficient completion of the reaction. Porosity is easily eliminated if the initial pores are very small. Grain growth during sintering can be better controlled if the initial size is small and uniform.

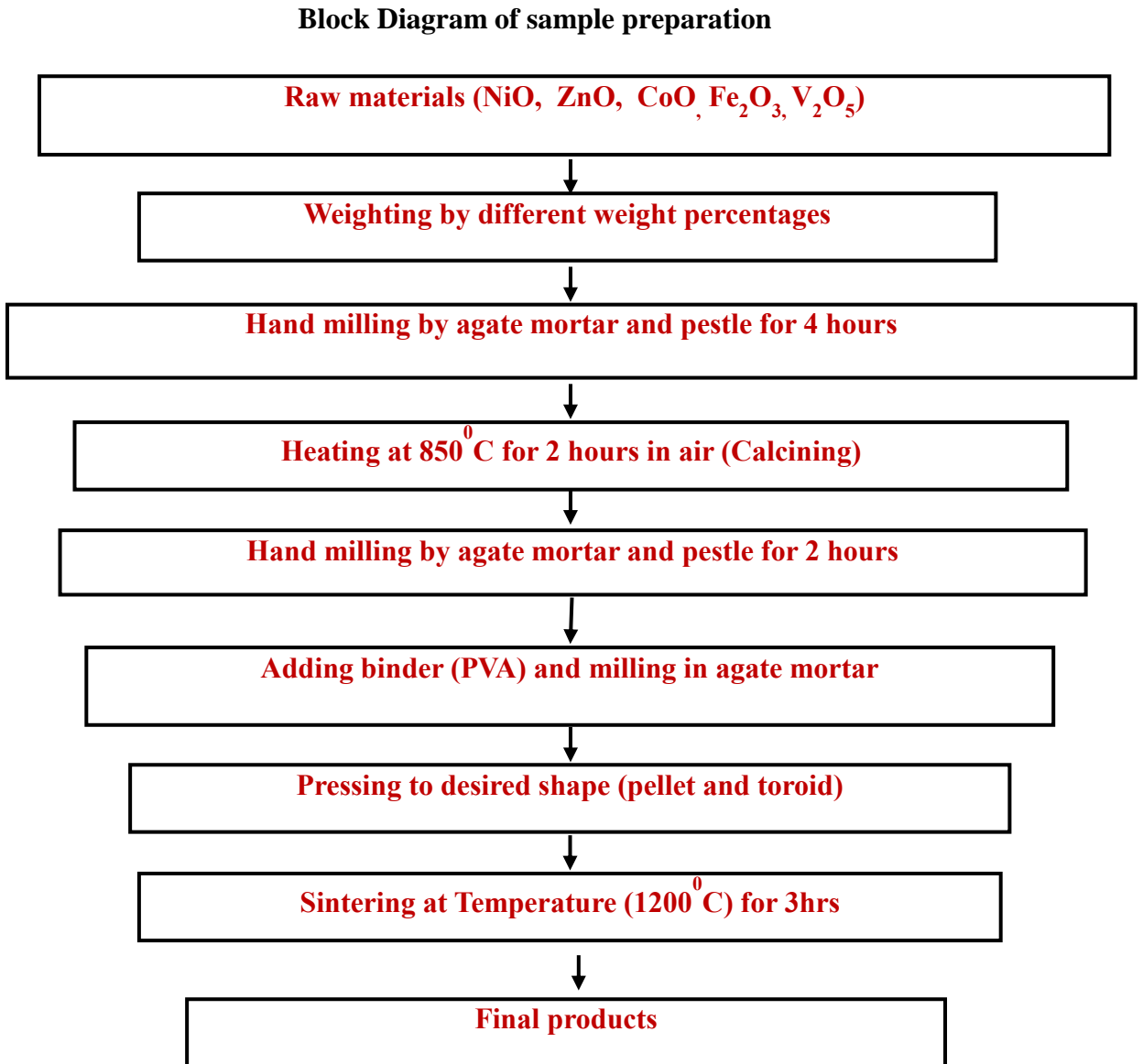


Fig. 3.11 Flow chart of the stages in preparation of spinel ferrite.

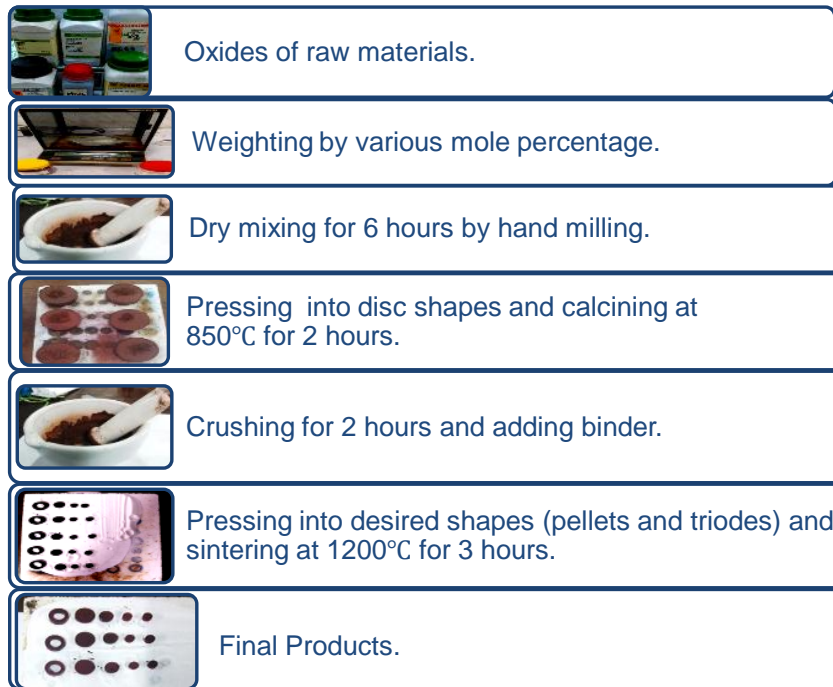


Fig. 3.12 Sample Preparation in Solid State Reaction Method.

A binder is usually added prior to compaction, at a concentration lower than 5wt%. Binder is polymers or waxes; the most commonly used binder in ferrite is polyvinyl alcohol. The binder facilitates the particles flow during compacting and increases the bonding between the particles, presumably by forming bonds of the type particle-binder-particle. During sintering, binders decompose and are eliminated from the ferrite. Pressures are used for compacting very widely but are commonly several tons per square inch (i.e., up to 10^8 Nm^{-2}).

Sintering is defined as the process of obtaining a dense, tough body by heating a compacted powder for a certain time at a temperature high enough to significantly promote diffusion, but clearly lower than the melting point of the main component. The driving force for sintering is the reduction in surface free energy of the powder. Part of this energy is transferred into interfacial energy (grain boundaries) in the resulting

polycrystalline body. The sintering time, temperature and the furnace atmosphere play very important role on the magnetic property of ferrite materials. The purposes of sintering process are:

1. To bind the particles tighter so as to impact sufficient to the product,
2. To density the material by eliminating the pores and
3. To homogenize the materials by completion the completing the reactions left unfinished in the Calcining step.

Sintering of crystalline solids is dealt by Coble and Burke who found the following empirical relationship regarding rate of grain growth:

$$d = k t^a$$

Where, d is the mean grain diameter, t is sintering time, a is about $1/3$ and k is a temperature dependent parameter.

Sintering is divided into three stages [33].

Stage 1: Contact area between particles increases.

Stage 2: Porosity changes from open to closed porosity.

Stage 3: Pore volume decreases, grains grow.

In the initial stage, neighboring particles form a neck by surface diffusion and presumably also at high temperatures by an evaporation-condensation mechanism. Grain growth begins during the intermediate stage of sintering. Since grain boundaries are the sinks for vacancies, grain growth tends to decrease the pore elimination rate due to the increase in distance between pores and grain boundaries, and by decreasing the total grain boundary surface area. In the final stage growth is considerably enhanced and the remaining pores may become isolated.

few charts for the synthesis of materials by the solid-state reaction route is illustrated in Fig.3.12.

3.1.5 Preparation of the Present Samples

The $\text{Ni}_{0.62}\text{Co}_{0.03}\text{Zn}_{0.35}\text{Fe}_2\text{O}_4 + x\text{V}_2\text{O}_5$ (where $x = 0.0, 0.5, 1.0,$ and $1.5\text{wt}\%$) samples were synthesized using the standard solid state reaction technique which discussed in section3.2. Powder of NiO, CoO, ZnO and Fe_2O_3 were used as raw materials. Stoichiometric amount of required powders were mixed thoroughly and then calcined at 850°C for 2 hours. The calcined powders were mixed with different proportional V_2O_5 wt% (0.0, 0.5, 1.0, 1.5wt%). Then, mixed PVA (poly vinyl alcohol) than pressed 15KN pressure into toroid shaped also pressed 20KN and 10KN into pellet shaped samples shown in Fig.3.14. The samples were sintered at 1200°C temperature in air for 4 hours. The temperature ramp was $10^\circ\text{C}/\text{minute}$ for both cooling and heating.

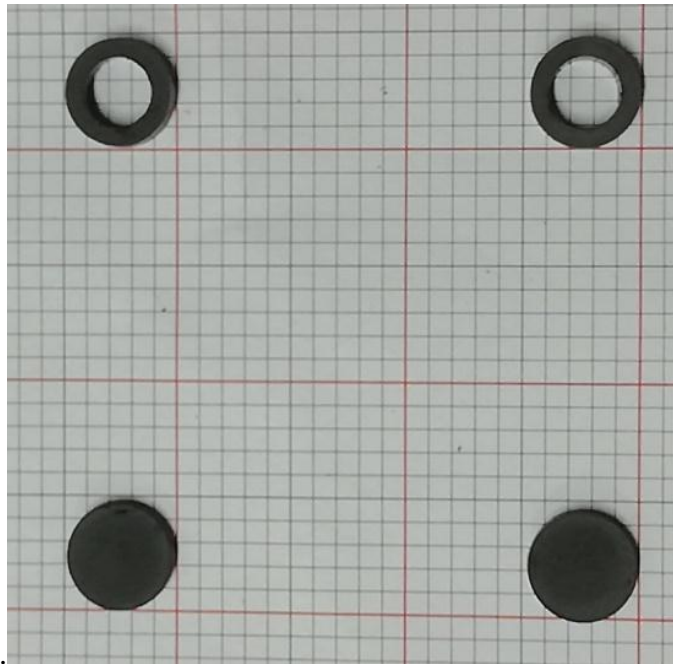


Fig.3.14 Toroid and Cylindrical shaped samples.

3.2 Characterizations

3.2.1 The X-ray Diffraction

The X-ray diffraction (XRD) provides precise knowledge of the lattice parameter as well as the substantial information on the crystal structure of the material under study. XRD is one of the most effective tools for the determination of phase in a sample. X-rays are the electromagnetic waves whose wavelengths are in the neighborhood of 1Å . The wavelength of an X-ray is thus of the same order of magnitude as the lattice constant of crystals. Whenever X-rays are incident on a crystal surface, they are reflected from it. This is called Bragg reflection. If a beam of monochromatic radiation of wavelength λ incident on a periodic crystal plane at an angle θ and is diffracted in the same angle, this event abides by the celebrated Bragg's law which is given below

$$2d\sin\theta = n\lambda \quad (3.1)$$

Here d is the distance between crystal planes, and n is positive integer. Bragg's law also suggests that the diffraction is only possible when $\lambda < 2d$ [18]. X-ray diffraction (XRD) is a versatile non-destructive analytical technique for identification and quantitative determination of various crystalline phases of powder or solid samples of any compound. A PHILIPS X Pert PRO X-ray diffraction system was used to get X-ray data for the samples at the Materials Science Division, Atomic Energy Center, Dhaka, which is a sophisticated X-ray diffractometer installed very recently. The powder diffraction technique was used with a primary beam power of 40 kV and 30mA for Cu radiation. A nickel filter was used to reduce Cu- K_{α} radiation and finally Cu- K_{α} radiation was only used as the primary beam. A $(\theta - 2\theta)$ scan was taken from 15° to 75° to get possible fundamental peaks of the sample with the sampling pitch of 0.02° and time for each step data collection was 1.0 sec. Both the programmable divergence and receiving slits were used to control the irradiated beam area and output intensity from the sample respectively.



Fig. 3.15 X-ray diffraction system

An anti-scatter slits were used just after the sample holder to reduce air scattering. Two solar slits were used just after the tube and in front of the detector to get parallel beam only. Data was analyzed using computer software "X PERT HIGHSCORE".

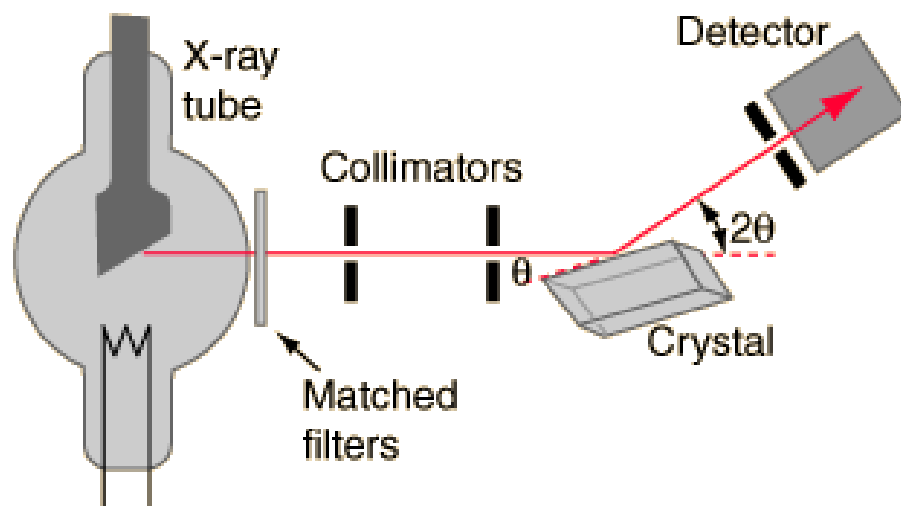


Fig. 3.16 A basic instrument for the Bragg spectrometer.

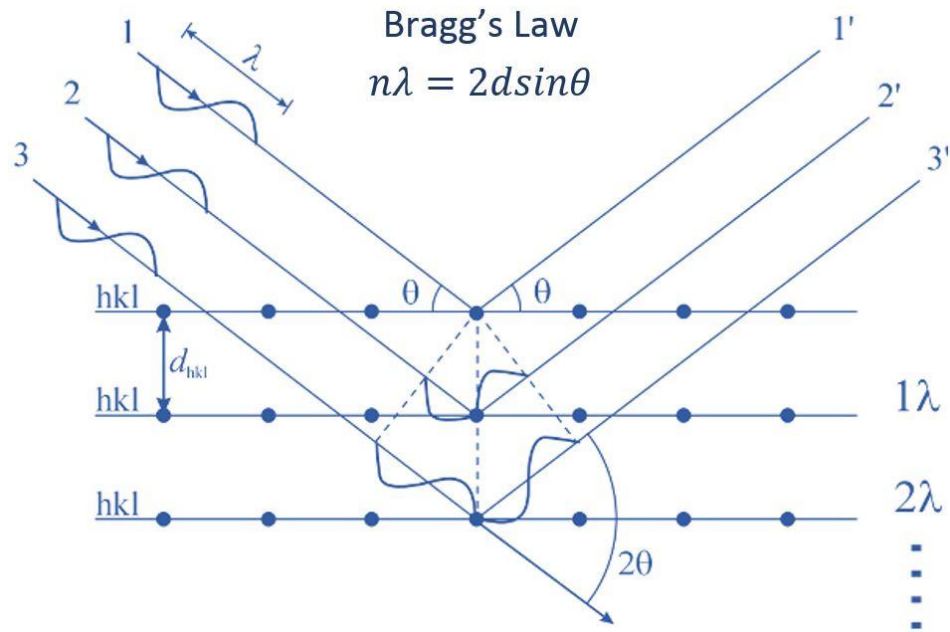


Fig.3.17 Geometry of the incident X-rays impinging the sample satisfying Bragg's law.

3.2.2 Interpretation of the XRD Data

The XRD data consisting of θ_{hkl} and d_{hkl} values corresponding to the different crystallographic planes are used to determine the structural information of the samples like lattice parameter and constituent phase.

The lattice parameter for each peak of each sample was calculated by using the formula:

$$a = d_{hkl} \times \sqrt{(h^2 + k^2 + l^2)} \quad (3.2)$$

Where, h, k and l are the indices of the crystal planes. To determine the exact lattice parameter for each sample, Nelson-Riley method was used. The Nelson-Riley function $F(\theta)$, can be written as

$$F(\theta) = \frac{1}{2} \left(\frac{\cos^2\theta}{\sin\theta} + \frac{\cos^2\theta}{\theta} \right) \quad (3.3)$$

Now drawing the graph of 'a' vs $F(\theta)$ and using linear fitting of those points will give us the lattice parameter a_0 . This is the value of 'a' at $F(\theta) = 0$.

3.2.3 X- Ray density and bulk density determination

X-ray density ρ_x was also calculated using the lattice parameter. The relation between ρ_x and a is as follows:

$$\rho_x = \frac{8M}{Na^3} \text{ gcm}^{-3} \quad (3.4)$$

Where, N is the Avogadro's number ($6.02 \times 10^{23} \text{ mol}^{-1}$), M is the molecular weight.

The bulk density, ρ_B is measured by the formula [34],

$$\rho = \frac{M}{V} \quad (3.5)$$

Where, M is the mass of the disc sample and V its volume.

Porosity (P%) in percentage was calculated using the

$$P = \left(1 - \frac{\rho_B}{\rho_x}\right) \quad (3.6)$$

3.2.4 The study of Field Emission Scanning Electron Microstructure

Sensitivity of electrical and magnetic properties depends on the microstructure of the ferrite sample. Permeability is directly proportional to grain size, At least up to a critical diameter of the grains permeability increases monotonically. Density and resistivity depends on the porosity of the sample. So study of microstructure is necessary for making prediction about the result of permeability and resistivity. The SEM microstructure of samples sintered at 1200°C was studied by Scanning Electron Microscope. To observe the microstructure, the ferrite samples were polished with fine Al_2O_3 powder followed by thermal etching from $800\text{-}900^\circ\text{C}$ for all samples. When the etching was completed, the grains were seen clearly by the SEM. The average grain size was calculated by the linear intercept method.



Fig. 3.18 Field Emission Scanning Electron Microscope (FESEM) setup.

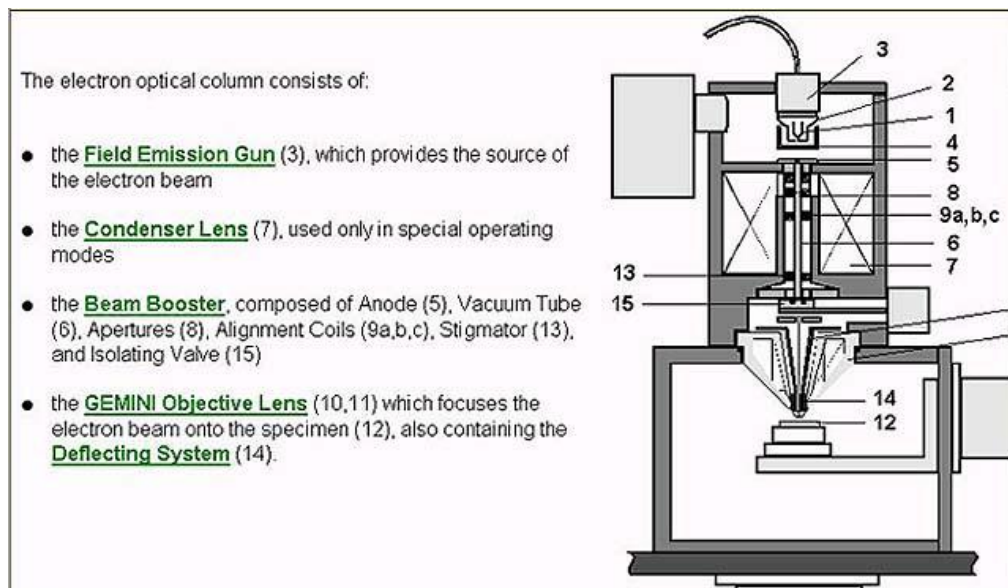


Fig. 3.19 A basic instrument for SEM.

3.2.5 Energy-Dispersive X-ray Spectroscopy

Energy-dispersive X-ray spectroscopy (EDS or EDX) is typically a quantitative analytical technique which is used for the chemical characterization or elemental analysis of a sample. EDX can be used to determine the chemical elements which are present in a given sample. It can also be used to estimate the relative abundance of each element in the specimen.

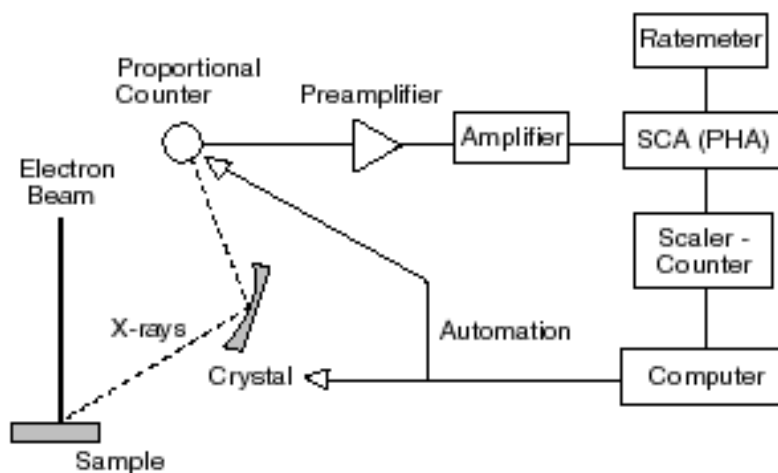


Fig.3.20 A basic instrumental setup for EDX.

A typical setup for an energy dispersive X-ray fluorescence spectrometer is shown in Fig 3.20. In this technique, a beam of charge particles such as a beam of X-rays, electrons or protons having high energy is focused into the studied sample. At rest, electrons of an atom in the sample are in the ground state (unexcited). Due to the high energy incident beam an electron in an inner shell (lower energy shell) may be excited and ejected from the shell leaving behind an electron hole at the place where the electron was. Generally, an electron from an outer energy level (higher energy shell) fills the hole. As a result, a characteristic X-ray may be released having energy equal to the energy difference between the higher energy level and the lower energy level. An energy-dispersive spectrometer is used to measure the number and energy of the emitted X-rays from the sample. Since the energies emitted as the form of X-rays are characteristic of the

difference in energy between the two energy levels and of the atomic structure of the emitted elements, EDS is used for elemental composition of the sample to be measured [35]. The characteristic X-ray generation process from a specimen is illustrated in Fig. 3.21.



Fig. 3.21 Characteristic X-ray Generation Process.

However, the accuracy of EDX analysis is affected by many factors such as nature of the sample, overlapping X-ray emission peaks etc. Hence it requires generally a quantitative correction approach. These approaches are sometimes referred to as the matrix correction. EDX analysis can be carried out by using a typical SEM/FESEM. The basic principle involved in this case is similar as described above. In this case high energy electron beam is used to stimulate the electrons of an atom in a specimen. In this thesis, the compositional study of the selected samples are carried out by using the EDX system supplied with the FESEM (JEOL, JSM-7600F) as shown in Fig.3.18.

3.2.6 Curie Temperature (T_c) Measurement

Curie temperature measurement is one of the most important measurements for magnetic materials. Curie temperature provides substantial information on magnetic states of a substance in respect of the strength of exchange interaction. So, the

determination of Curie temperature accurately is of great importance. Curie temperature measurements were done by using Agilent precision impedance analyzer (Agilent 4294A), with a small oven and a thermocouple based thermometer. The temperature dependent permeability was measured by using induction method. The specimen formed the core of the coil. We used a 100 kHz AC signal of 100 mV. By varying temperature, inductance of the coil as a function of temperature was measured. Dividing this value by L_0 (inductance of the coil without core material), permeability of the sample was determined. When the magnetic state inside the ferrite sample changes from ferromagnetic to paramagnetic, the permeability falls sharply. From this sharp fall at specific temperature, the Curie temperature is determined. This is the basic principle used in our experimental set up. The number of turns in each coil is 5. The sample thus wound is kept in the middle position of a tubular oven with a thermocouple placed close to the sample. The thermocouple measures the temperature inside oven and also of the sample. The sample is kept just in the middle part of the cylindrical oven so that temperature gradient is minimized. The temperature of the oven is raised slowly. If the heating rate is very fast then temperature of the sample may not follow the temperature inside the oven and there can be misleading information on the temperature of the samples. So, a slow heating rate can eliminate this problem. Also a slow heating ensures accuracy in the determination of Curie temperature. The oven was kept thermally insulated from the surroundings. Actually Curie Temperature was measured from the temperature dependence of initial permeability.

3.2.7 Saturation Magnetization Measurement

Magnetization is defined as the magnetic moment per unit volume. There are various techniques of measuring magnetization of a substance. Vibrating sample magnetometer, as the name implies, vibrate the sample as part of the measurement process. This provides the flux meter element of the system with the dynamic component which it requires to make the measurement.



Fig. 3.22 Vibrating Sample Magnetometer.

The applied field is changed so, at each measurement point the field is static and hence no eddy currents to cause problems. The objective when using a VSM or any other type of magnetic characterization system is to obtain the dependence of the magnetization on the applied field. The sample, usually a sphere or small disc, is cemented to the lower end of a rod, the other end of which is fixed to a mechanical vibrator. Current through the vibrator and vibrate the rod at about 37Hz with amplitude of about 7V in a direction at right angles to the magnetic field. The oscillating magnetic field of the sample induces an alternation emf in the direction coils. The vibrating rod also carries a reference specimen, in the form of a small permanent magnet near its upper end; the oscillating field of this induces another emf in two reference coils. The two voltage form two sets of coils are compared, and the difference is proportional to the magnetic moment of the sample. The magnetization measurement was performed (0- 1500 G) magnetic field for all samples.

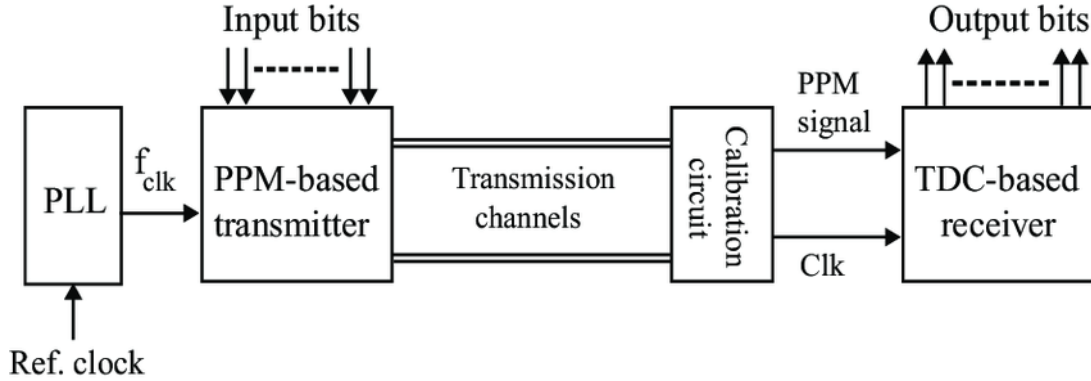


Fig.3.23 A block diagram of PPMS setup.

3.2.8 Complex Permeability Measurement

For high frequency application, the desirable property of a ferrite is the high permeability with low loss. The present goal of most of the recent ferrite researchers is to fulfill this requirement. Permeability is namely defined as the proportional constant between the magnetic field induction B and applied field intensity H [36]:

$$\mathbf{B} = \mu \mathbf{H} \quad (3.7)$$

If a magnetic material is subjected to an AC magnetic field as given below;

$$\mathbf{H} = \mathbf{H}_0 e^{i\omega t} \quad (3.8)$$

Then, it is observed that the magnetic flux density B experiences a delay. This delay is caused due to presence of various losses and is thus expressed as

$$\mathbf{B} = \mathbf{B}_0 e^{i(\omega t - \delta)} \quad (3.9)$$

where δ is the phase angle and marks the delay of B with respect to H . The permeability is then given by

$$\mu = \frac{B}{H} = \frac{B_0 e^{i(\omega t - \delta)}}{H_0 e^{i\omega t}} = \frac{B_0 e^{-i\delta}}{H_0} = \mu' - i\mu'' \quad (3.10)$$

$$\text{where } \mu' = \frac{B_0}{H_0} \cos\delta, \mu'' = \frac{B_0}{H_0} \sin\delta \quad (3.11)$$

The real part μ' of complex permeability μ as expressed in equation (3.11) represents the component of B which is in phase with H, so it corresponds to the normal permeability. If there are no losses, we should have $\mu = \mu'$. The imaginary part μ'' corresponds to that part of B which is delayed by phase angle ranging upto 90° from H. The presence of such a component requires a supply of energy to maintain the alternating magnetization, regardless of the origin of delay. The ratio of μ'' to μ' , as is evident from equation (3.15) gives

$$\frac{\mu''}{\mu'} = \frac{\frac{B_0 \sin\delta}{H_0}}{\frac{B_0 \cos\delta}{H_0}} = \tan\delta \quad (3.12)$$

This $\tan\delta$ is called the Loss Factor or Loss tangent. The Q-factor or quality factor is defined as the reciprocal of this loss factor, i.e.

$$Q = \frac{1}{\tan\delta} \quad (3.13)$$

Measurements of permeability normally involve the measurements of the change in self-inductance of a coil in presence of the magnetic core. The behavior of a self-inductance can now be described as follows. Suppose we have an ideal lossless air coil of inductance, L_0 . On insertion of magnetic core with permeability μ , the inductance will be μL_0 . The complex impedance Z of this coil [32] can be expressed as

$$Z = R + jX = j\omega L_0 \mu = j\omega L_0 (\mu' - j\mu'') \quad (3.14)$$

where the resistive part is

$$R = \omega L_0 \mu'' \quad (3.15)$$

and the reactive part is

$$X = \omega L_0 \mu' \quad (3.16)$$

The radio frequency (RF) permeability can be derived from the complex impedance of a coil Z (equation 3.19). The core is usually toroidal to avoid demagnetization effects. The quantity L_0 is derived geometrically. The frequency characteristics of the Ni-Co-Zn ferrite + xV_2O_5 samples i.e. the permeability spectra were investigated using Wayne Kerr Impedance Analyzer (6500B).



Fig. 3.24 Experimental setup of Wayne Kerr Impedance Analyzer (6500B).

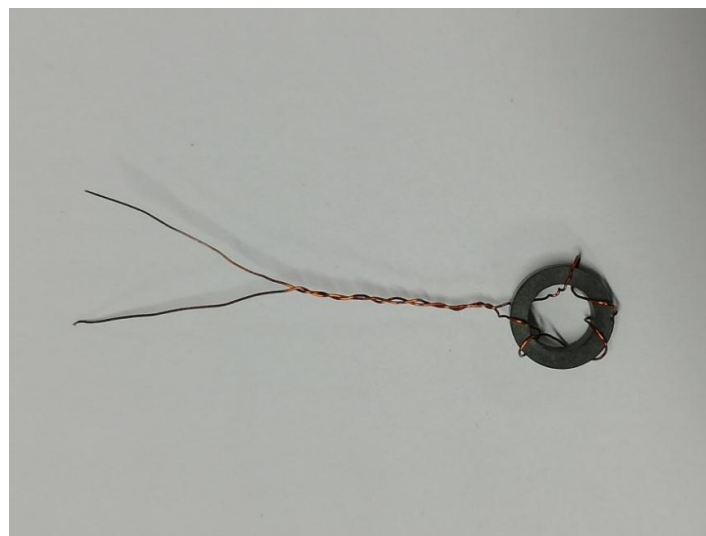


Fig. 3.25 Toroid shaped sample for the measurement of permeability.

The measurements of inductances were taken in the frequency range of 20Hz to 120MHz. The values of measured parameters such as inductance and loss tangent were obtained as a function of frequency. The real and the imaginary part of permeability are calculated. μ' is calculated by using the following formula:

$$L_s = L_0\mu' \quad (3.17)$$

And

$$\tan\delta = \frac{\mu''}{\mu'} \quad (3.18)$$

where L_0 is the self-inductance of the sample core and

$$L_0 = \frac{\mu_0 N^2 S}{\pi \bar{d}} \quad (3.19)$$

where L_0 is the inductance of the winding coil without the sample core and N is the number of turns of coil (here $N = 5$), S is the area of cross section of the toroid as given below

$$s = dh,$$

$$\text{where } d = \frac{(d_1 \sim d_2)}{2}, \quad (3.20)$$

$$h = \text{height}$$

$$\bar{d} = \frac{d_1 + d_2}{2} \quad (3.21)$$

By applying a comparatively small sinusoidal signal of amplitude A and frequency f to the capacitor, the displacement current I through the capacitor and the voltage V across the capacitor can be measurement by using an Impedance Analyzer and find the complex impedance Z from the Ohm's Law [38].

$$\frac{V}{I} = Z = R - jX = Z \quad (3.22)$$

$$X = \frac{1}{2\pi fC} \quad (3.23)$$

When the capacitor under test is small, the reactance X will be large and possibly affected by a parasitic resistance. On the other hand, if the capacitance under test is typically larger than the reactance will be small and likely to be affected by a series resistance. For making the above two equations simple, the admittance Y is found instead of the impedance.

$$\frac{1}{V} = \frac{1}{Z} = Y \quad (3.24)$$

$$Y = G + jB = Y \quad (3.25)$$

$$|Y| = \sqrt{(G^2 + B^2)} \quad (3.26)$$

$$B = 2\pi fC \quad (3.27)$$

$$R_p = \frac{1}{G} \quad (3.28)$$

In the above equations, B is the susceptibility measurement in Siemens and G stands for the conductance measured also in Siemens. All of these equations are done inside the Impedance Analyzer and the capacitance C is displaying along with the parasitic parallel resistance R_p . Other useful parameters includes the quality factor Q and the dissipation or loss factor D . These two parameters provide a metric for the ratio of parasitic resistance and capacitance. The quality factor can be expressed as,

$$Q = \frac{1}{D} = \frac{|B|}{G} \quad (3.29)$$

If the capacitor is ideal then no parasitic resistance will present. As a result, the quality factor Q will be infinity. Hence, under this condition low dissipation factor and high quality factor is mostly desirable. The value of the dielectric constant ϵ' can easily be evaluated by using the parallel plate capacitor equation when the capacitance is found.

$$\epsilon' = \frac{Cd}{\epsilon_0 A} \quad (3.30)$$

Where, C is the capacitance of the dielectric measurement in “F”, d is the thickness of the shaped sample measurement in “m”, ϵ_0 is the permittivity of the free space ($8.854 \times 10^{-12} \text{ Fm}^{-1}$) and A is the cross sectional area of the electrode measured in “m²”.

3.2.9 Electrical Resistivity Measurement

Electrical resistivity of the samples has been measured by two probe method. Samples were prepared by sintering temperature of 1200°C. The samples were polished with the help of emery paper with grit size 800 and 1000 successively. Then silver past was added to the both sides of the polished samples together with two thin copper wires of 100 micron diameter. The resistivity has been calculated using the formula

$$\rho = \frac{RA}{l} \quad (3.31)$$

where, ρ is the resistivity, l and A are the thickness and the area of the sample, respectively.

3.2.10 Dielectric Constant Measurement

A dielectric material is typically an insulator which is polarized when subjected to an applied electric field. Basically the study of dielectric properties involves the storage and dissipation of electric and magnetic energy in materials. Typically the measurement of dielectric constant involves the measurement of capacitance C_0 of a test capacitor with vacuum between its plates. Then using the same capacitor and maintaining the same distance between its plates, the capacitance C with a dielectric material between the plates is measured. The simplest capacitor structure is a pair of parallel conducting plates separated by a medium called the dielectric. The value of the capacitance between the plates is given by the equation [39].

$$C = \frac{\epsilon A}{d} \quad (3.32)$$

where, A is the area of the plates, d is the separation between the plates and ϵ is the absolute permittivity of the dielectric, which is a measure of the electrostatic energy stored within it and therefore dependent of the material. The dielectric constant of an

insulating material is therefore numerically the ratio of the capacitance of a capacitor containing that material to the capacitance of the same electrode system with vacuum replacing the insulation as the dielectric medium. The dielectric constant of the medium (also known as the relative permittivity) is defined as

$$\epsilon_r = \frac{\epsilon}{\epsilon_0} \quad (3.33)$$

where ϵ_0 is the permittivity of free space, which has value of $8.85 \times 10^{-12} \text{ Fm}^{-1}$. There are several methods available for measurement of dielectric properties of the material. The instruments that are used to employ those techniques have some common parts such as, test fixtures to hold the specimen under investigation, precise instrument section and software that makes the whole measurement process easier and display the results. In the present study, a precision impedance analyzer is used for investigating the dielectric properties of the selected samples. The basic function and working principle of an impedance analyzer is discussed below.

3.2.11 Impedance Spectroscopy

For investigating the electrical properties of materials the complex spectroscopy is a very powerful tool. There are many advantages of this technique. The main advantages include,

- i) The technique involves comparatively simple electrical measurements.
- ii) The measurement can be done by using arbitrary electrodes.
- iii) By using this technique the resistance of the grain and grain boundaries in most of the polycrystalline materials can be separated simply.

Typically a Wheatstone-bridge type setup (LCR meter or Impedance Analyzer) is used for ac measurements. In this technique, the resistance R and capacitance C of the specimen are measured and balanced against variable resistors and capacitors. The technique in which the impedance $|Z|$ and the phase difference (θ) between the voltage and current are measured as a function of frequency for the given specimen is known as impedance

spectroscopy. For the analysis of obtained data an plot (a plot between the imaginary part of the impedance $Z'' = |Z|\sin\theta$ and the real part $Z' = |Z|\cos\theta$ on a complex plane) is drawn. Generally an impedance plot with linear scale is used for analyzing the equivalent circuit. Impedance plot of a pure capacitor is a straight line coincides with the imaginary axis and that of pure resistor defines a point on the real axis. The following relation is used to express the impedance of a parallel RC combination [40].

$$Z^* = Z' - jZ''$$

$$Z^* = \frac{R}{(1+j\omega RC)}$$

After simplification, we get

$$\left(Z' - \frac{R}{2}\right)^2 + (Z'')^2 = \left(\frac{R}{2}\right)^2 \quad (3.34)$$

This equation represents a circle of radius $\frac{R}{2}$ and centre at $\left(\frac{R}{2}, 0\right)$. Therefore, a plot between Z' and Z'' will represent a semicircle of radius $\frac{R}{2}$ as shown in fig.3.26 (a). This plot is often known as Nyquist plot. The time constant of a simple circuit can be written as,

$$\tau = RC = \frac{1}{\omega_0} \quad (3.35)$$

This relation to the relaxation time of the specimen and the characteristic frequency lies at the peak of the semi-circle. At high frequency, the impedance plot exhibits an arc related to the bulk property of an ideal specimen. Whereas an arc at low frequency corresponds to the grain boundary behavior and a spike at the lowest frequency is related to the electrode effect. A typical impedance plot and the equivalent circuit for a polycrystalline material are illustrated in Fig.3.26 (b). In this thesis, a precision Impedance Analyzer (Wayne Kerr Impedance Analyzer, 6500B) is used for the measurement of real (Z') and imaginary (Z'') part of the complex impedance as a function of frequency at room temperature.

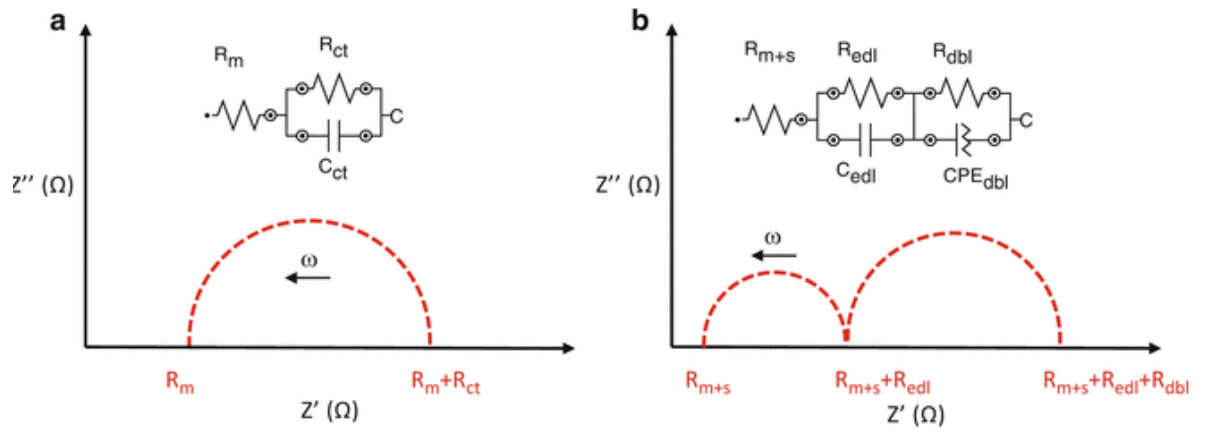


Fig. 3.26 (a) An impedance plot with the corresponding equivalent circuit and (b) Impedance plot an ideal polycrystalline sample with the equivalent circuit.

CHAPTER 4 RESULTS AND DISCUSSION

4.1 Structural Property of V₂O₅ Added Ni-Co-Zn Ferrites

The crystal structure of V₂O₅ added Ni-Co-Zn ferrites were studied using an X-ray diffraction (XRD) method for the compositions of Ni_{0.62}Co_{0.03}Zn_{0.35}Fe₂O₄ + xV₂O₅, where, x= 0.0, 0.5, 1.0, and 1.5wt %.

4.1.1 X-ray diffraction

Fig.4.1 shows the X-ray diffraction patterns of V₂O₅ added Ni-Co-Zn ferrites having different compositions sintered at 1200°C for 3 hours.

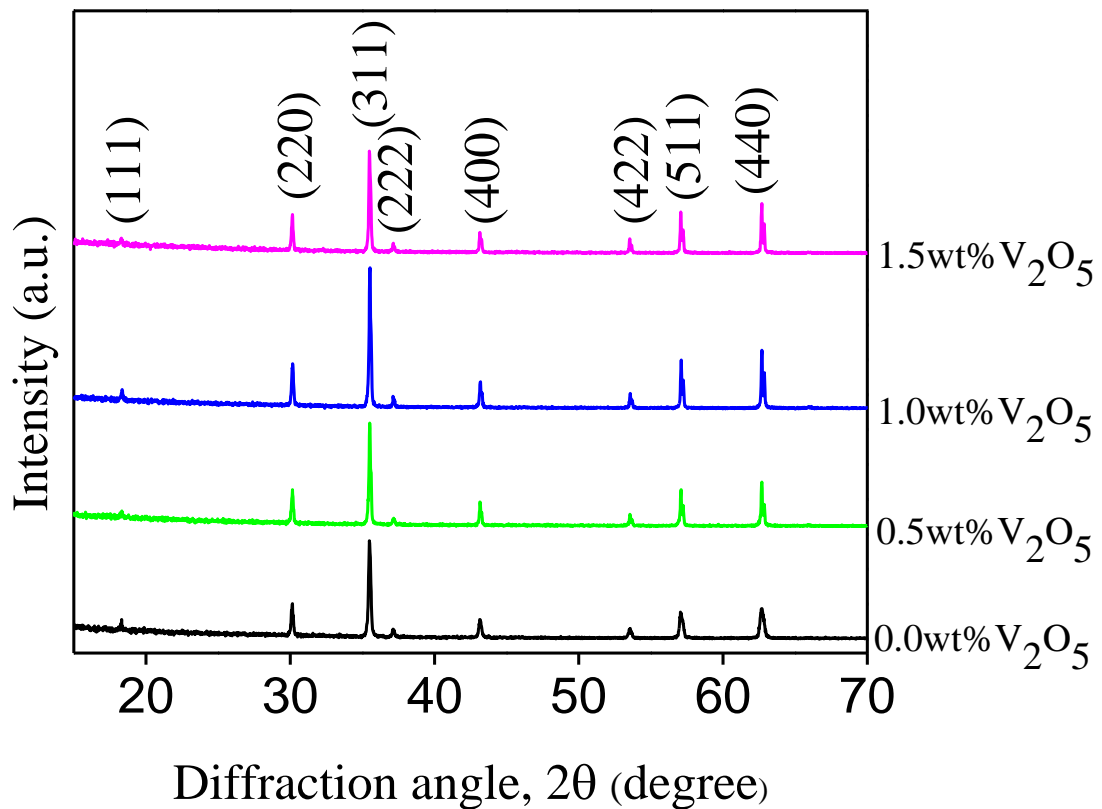


Fig.4.1 XRD patterns of Ni_{0.62}Co_{0.03}Zn_{0.35}Fe₂O₄ + xV₂O₅ sintered at 1200°C.

In these patterns, the reflection planes (111), (220), (311), (222), (400), (422), (511) and (440) were observed and it confirmed that all the prepared compositions were the spinel cubic structure [12]. In order to obtain the experimental lattice parameter, Nelson-Riley (N-R) function, $F(\theta)$ was used in this study [40]. For the calculation of the desired lattice parameter, the graph of apparent lattice parameter 'a' vs N-R function, $F(\theta)$ are given in fig.4.2. The Y-axis at $F(\theta) = 0$ gives the exact value of lattice parameters.

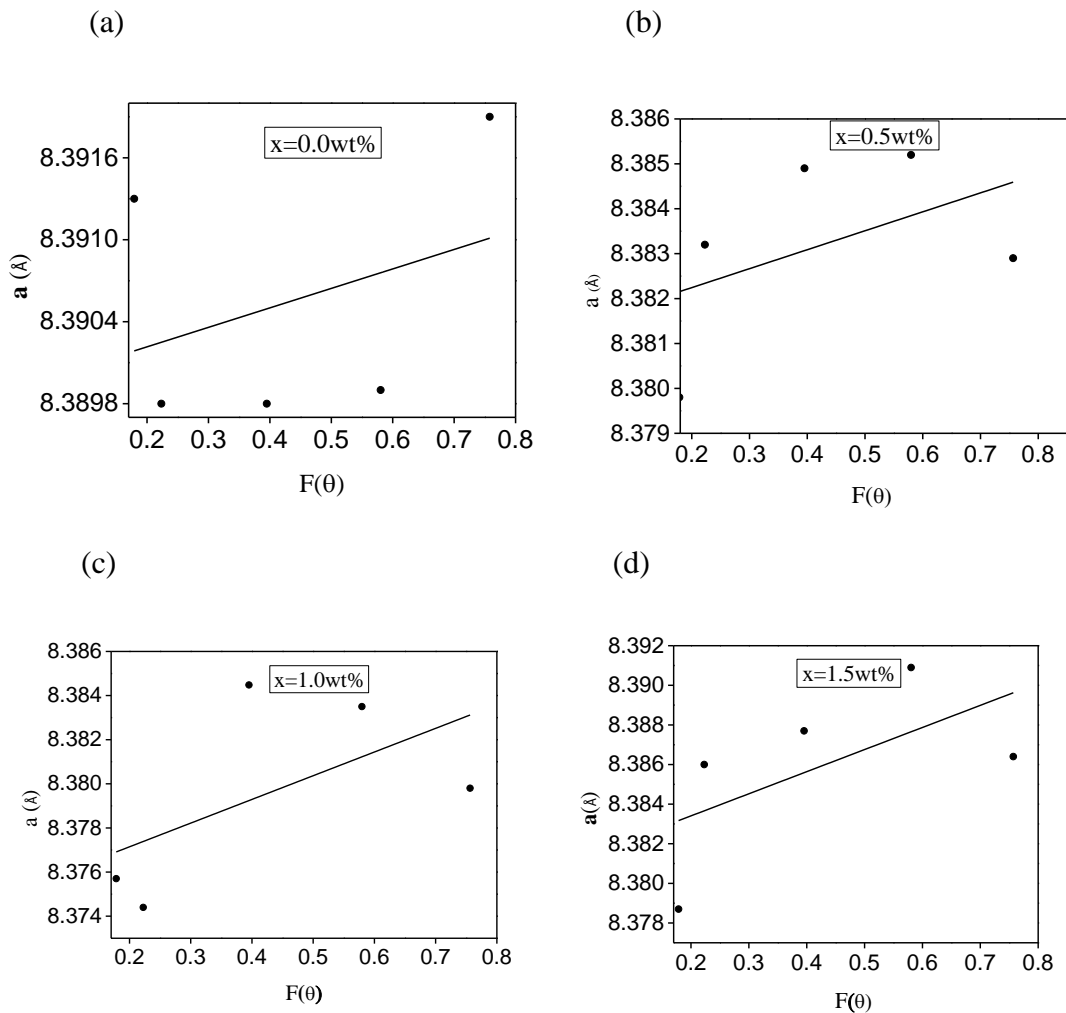


Fig.4.2 Variation of the apparent lattice parameter, a (Å) with $F(\theta)$ for V_2O_5 added Ni-Co-Zn ferrites having the compositions $Ni_{0.62}Co_{0.03}Zn_{0.35}Fe_2O_4+xV_2O_5$, where a) $x=0.0\text{wt}\%$, b) $x=0.5\text{wt}\%$, c) $x=1.0\text{wt}\%$ and d) $x=1.5\text{wt}\%$.

Fig.4.3 shows the variation of lattice parameters 'a' with the addition of V_2O_5 (wt%) for the sintering temperature 1200°C . It is observed that the lattice constant decreases slightly due to the addition of V_2O_5 . This may be happened due to the ionic radii deviation, since V^{5+} ions have smaller radius (0.59\AA) than that of Fe^{3+} (0.64\AA) and Ni^{2+} (0.69\AA) ions which turn to decrease of the lattice constant [10].

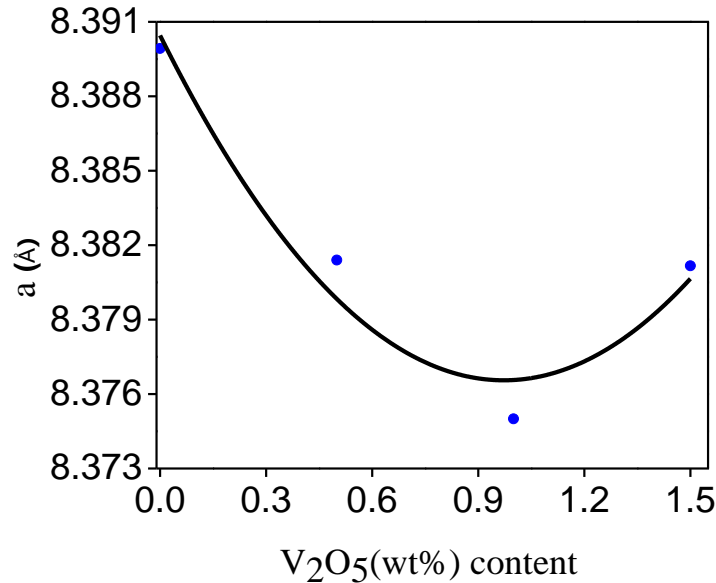


Fig.4.3 Variation of the experimental lattice parameters 'a' with V_2O_5 (wt%) contents.

The parameters such as x-ray density, bulk density, crystallite size and porosity were calculated using XRD data for all samples. The bulk density was increased from 4.1334 to 5.006 g/cc due to the addition of V_2O_5 wt%. This result is shown in fig.4.4. Fig 4.5 shows the variation X-ray density as function V_2O_5 content. It was found that the X-ray density was increased from 5.4420 to 5.5207 g/cc due to increase of V_2O_5 contents. Although X-ray density was found higher than that of the bulk density, but the deviation between X-ray and bulk densities is more at the lower contents of V_2O_5 additive. However this deviation is smaller at 1.5wt% V_2O_5 additive. This can be attributed to the fact of densification. The value of porosity (%) was found to decrease from 24.05 to 9.42 due to the addition of V_2O_5 (wt%) contents. This is given in fig.4.6. In addition, it was

observed that the crystallite size increases with increasing of amount of additive V_2O_5 and this is given in Table 4.1.

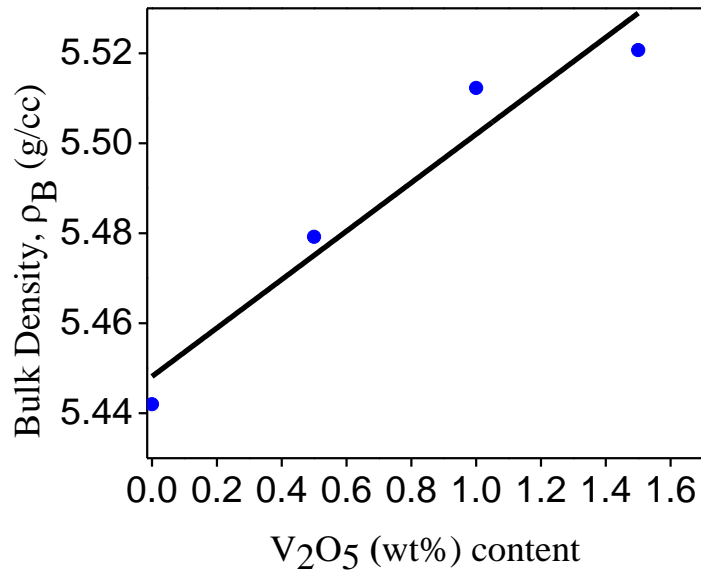


Fig.4.4 Variation of bulk density with V_2O_5 (wt%) contents.

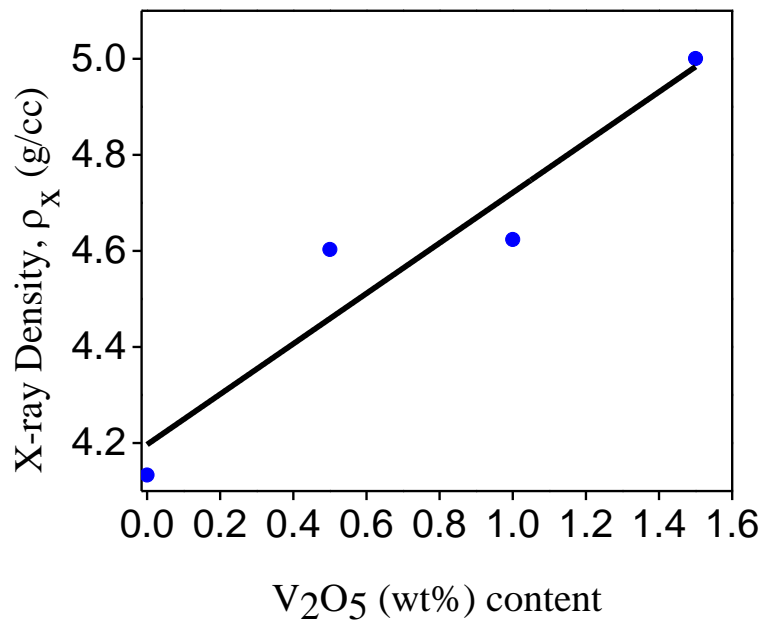


Fig. 4.5 Variation of X-ray density with V_2O_5 (wt%) contents.

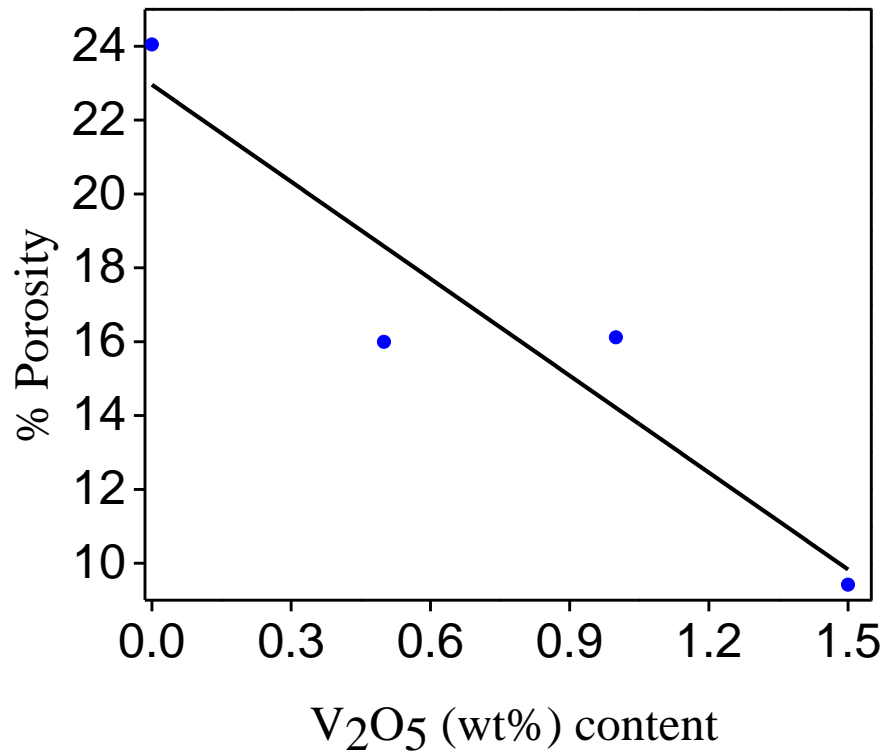


Fig.4.6 Variation of % porosity with V₂O₅ (wt%) contents.

Table 4.1 Crystallite size (t), Lattice parameter (a), X-ray density (ρ_x), Bulk density (ρ_B) and Porosity (P%) for the Ni_{0.62}Co_{0.03}Zn_{0.35}Fe₂O₄ + xV₂O₅ sintered at 1200°.

Compositions	T (nm)	a (Å)	ρ_x (g/cc)	ρ_B (g/cc)	(P)%
Ni _{0.62} Co _{0.03} Zn _{0.35} Fe ₂ O ₄	55.26	8.3899	5.442	4.133	24.05
Ni _{0.62} Co _{0.03} Zn _{0.35} Fe ₂ O ₄ +0.5wt% V ₂ O ₅	91.47	8.3814	5.479	4.602	16.00
Ni _{0.62} Co _{0.03} Zn _{0.35} Fe ₂ O ₄ +1.0wt% V ₂ O ₅	98.43	8.3750	5.512	4.650	15.60
Ni _{0.62} Co _{0.03} Zn _{0.35} Fe ₂ O ₄ +1.5wt% V ₂ O ₅	108.79	8.3811	5.520	5.000	9.42

4.2 Surface Morphology

The FESEM photomicrographs for the prepared samples are shown in fig.4.7. These photomicrographs were observed under the same magnification and scale for all samples.

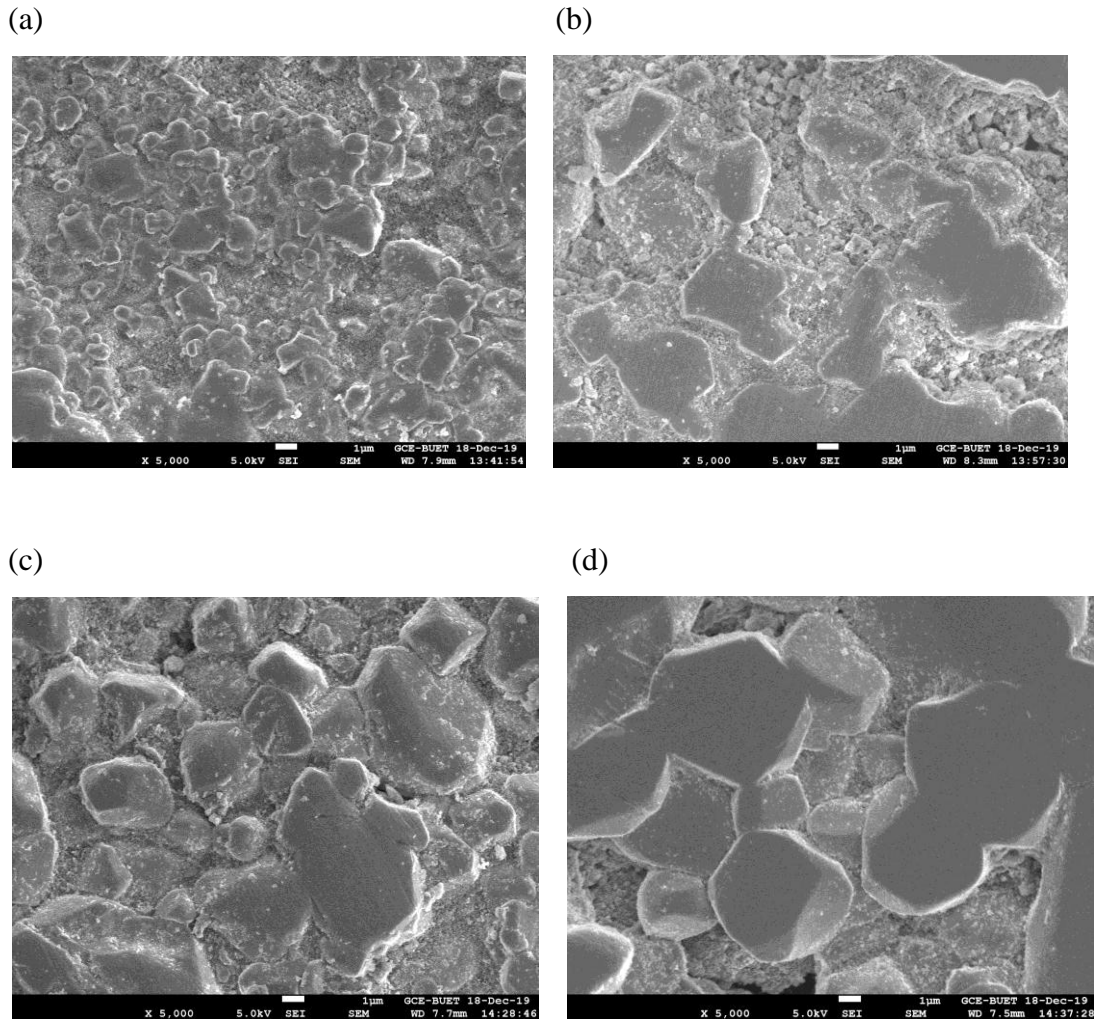


Fig.4.7 FESEM photomicrograph of $\text{Ni}_{0.62}\text{Co}_{0.03}\text{Zn}_{0.35}\text{Fe}_2\text{O}_4 + x\text{V}_2\text{O}_5$, sintered at 1200°C where (a) $x=0.0\text{wt}\%$, (b) $x=0.5\text{wt}\%$, (c) $x=1.0\text{wt}\%$ and (d) $x=1.5\text{wt}\%$.

The calculated value of the average grain size is shown in Table 4.2. It is observed that the average grain size of the Ni-Co-Zn ferrites strongly depend on the amount of V_2O_5 (wt%) contents. It is noticed from the microstructure that V_2O_5 addition has

substantial role in the growth of grains sintered at $T_s=1200^\circ\text{C}$. A four times increase of grain size from $1.5\mu\text{m}$ for the sample $x=0.0\text{wt}\%$ V_2O_5 to $6.8\mu\text{m}$ for that of $x=1.5\text{wt}\%$ V_2O_5 is evident. The effect of V_2O_5 on the sintering mechanism and grain growth is clearly reflected from this study. This has been reflected in the increase of density or decrease of porosity with the addition of V_2O_5 .

Table 4.2 Average grain size, D of $\text{Ni}_{0.62}\text{Co}_{0.03}\text{Zn}_{0.35}\text{Fe}_2\text{O}_4 + x\text{V}_2\text{O}_5$ sintered at 1200°C .

Compositions	Grain size, D (μm)
$\text{Ni}_{0.62}\text{Co}_{0.03}\text{Zn}_{0.35}\text{Fe}_2\text{O}_4$	1.5
$\text{Ni}_{0.62}\text{Co}_{0.03}\text{Zn}_{0.35}\text{Fe}_2\text{O}_4+0.5\text{wt}\%\text{V}_2\text{O}_5$	2.9
$\text{Ni}_{0.62}\text{Co}_{0.03}\text{Zn}_{0.35}\text{Fe}_2\text{O}_4+1.0\text{wt}\%\text{V}_2\text{O}_5$	5.0
$\text{Ni}_{0.62}\text{Co}_{0.03}\text{Zn}_{0.35}\text{Fe}_2\text{O}_4+1.5\text{wt}\%\text{V}_2\text{O}_5$	6.8

4.3 Elemental Analysis

The quantitative elemental analysis EDX spectra of $\text{Ni}_{0.62}\text{Co}_{0.03}\text{Zn}_{0.35}\text{Fe}_2\text{O}_4+x\text{V}_2\text{O}_5$ samples (where $x=0.0, 0.5, 1.0, 1.5\text{wt}\%$) are shown in fig.4.8. By the red colour indicated the location on FESEM images where the corresponding EDX were taken in this study. The compositions with EDX results have agreed with the composition calculated from formula without other impurity element. Therefore, the solid state reaction method in this reaserch work is an appropriate for performing good stoichiometry in the spinel ferrite. Data of elemental analysis for studing compositions of $\text{Ni}_{0.62}\text{Co}_{0.03}\text{Zn}_{0.35}\text{Fe}_2\text{O}_4+x\text{V}_2\text{O}_5$ are given in Table 4.3. It is observed that the bulk material are fully stoichiometric. The presence of O, V, Fe, Co, Ni and Zn are ensured in the spinel ferrites samples.

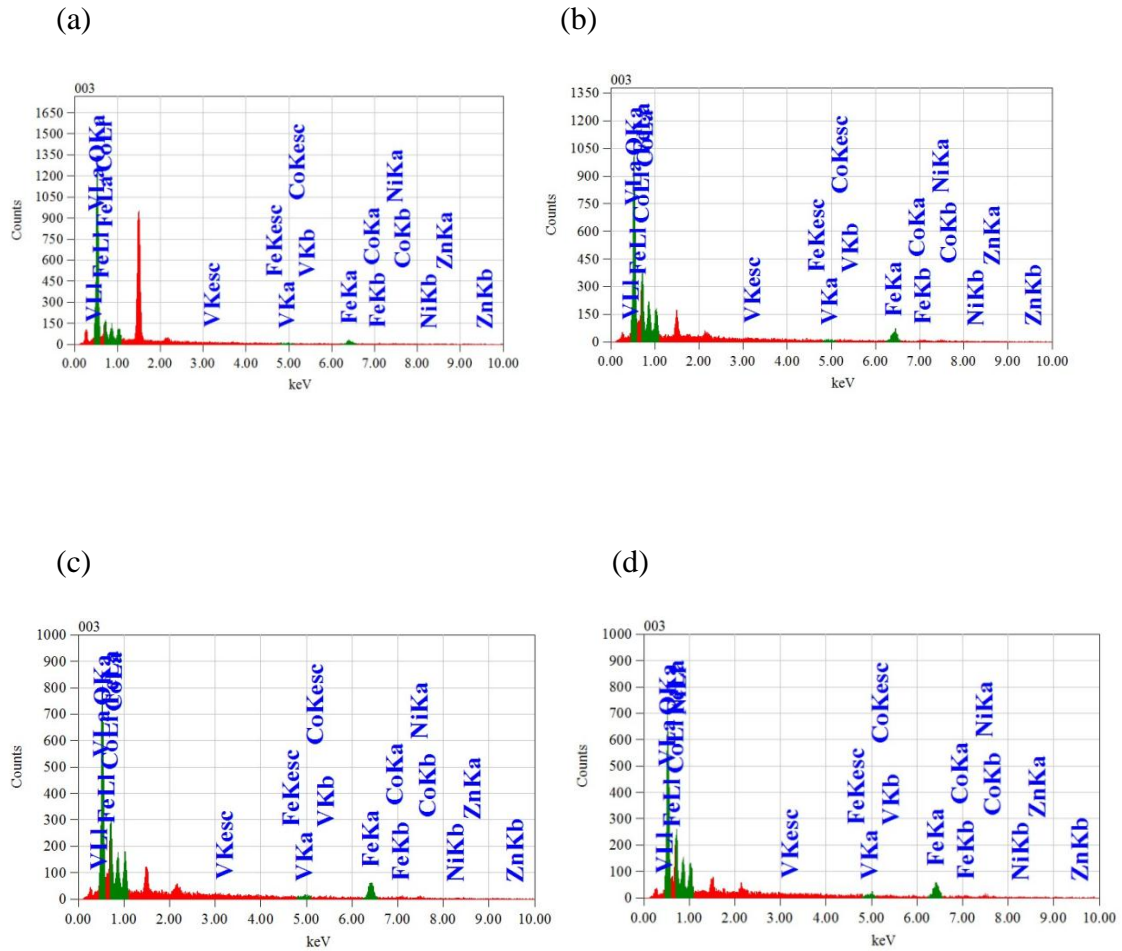


Fig.4.8 EDX spectra of $\text{Ni}_{0.62}\text{Co}_{0.03}\text{Zn}_{0.35}\text{Fe}_2\text{O}_4 + x\text{V}_2\text{O}_5$, where (a) $x=0.0\text{wt}\%$, (b) $x=0.5\text{wt}\%$, (c) $x=1.0\text{wt}\%$ and (d) $x=1.5\text{wt}\%$, sintered at 1200°C .

Table 4.3 Data of EDX for $\text{Ni}_{0.62}\text{Co}_{0.03}\text{Zn}_{0.35}\text{Fe}_2\text{O}_4 + x\text{V}_2\text{O}_5$ spinel ferrites.

Sample	Elements	Mass %	Atom %
$\text{Ni}_{0.62}\text{Co}_{0.03}\text{Zn}_{0.35}\text{Fe}_2\text{O}_4$	O	54.17	81.16
	V	0.00	0.00
	Fe	19.01	8.00
	Co	2.28	1.71
	Ni	17.27	6.46
	Zn	7.27	2.67
	Total	100.00	100.00
$\text{Ni}_{0.62}\text{Co}_{0.03}\text{Zn}_{0.35}\text{Fe}_2\text{O}_4 + 0.5\text{wt}\% \text{V}_2\text{O}_5$	O	33.70	64.08
	V	0.74	0.45
	Fe	30.88	16.50
	Co	2.24	2.13
	Ni	23.01	12.04
	Zn	9.43	4.80
	Total	100.00	100.00
$\text{Ni}_{0.62}\text{Co}_{0.03}\text{Zn}_{0.35}\text{Fe}_2\text{O}_4 + 1.0\text{wt}\% \text{V}_2\text{O}_5$	O	27.86	58.44
	V	0.79	0.58
	Fe	39.31	22.78
	Co	2.20	2.11
	Ni	19.24	10.75
	Zn	10.60	5.34
	Total	100.00	100.00
$\text{Ni}_{0.62}\text{Co}_{0.03}\text{Zn}_{0.35}\text{Fe}_2\text{O}_4 + 1.5\text{wt}\% \text{V}_2\text{O}_5$	O	26.83	57.01
	V	1.49	0.99
	Fe	36.34	22.12
	Co	3.75	2.16
	Ni	21.75	12.59
	Zn	9.84	5.12
	Total	100.00	100.00

4.4 Magnetic Properties

4.4.1 M-H curve at room temperature

The magnetization, M as a function of applied magnetic field strength, H for different compositions $\text{Ni}_{0.62}\text{Co}_{0.03}\text{Zn}_{0.35}\text{Fe}_2\text{O}_4 + x\text{V}_2\text{O}_5$ (where $x = 0.0, 0.5, 1.0, 1.5\text{wt}\%$) were studied at room temperature (300K). The obtained results are shown in fig4.9. The magnetization increases sharply with increasing of applied field for all samples. These magnetic fields are at ~ 72 Oe for $x = 0.0\text{wt}\%$ V_2O_5 , at $\sim x = 63$ Oe for $0.5\text{wt}\%$ V_2O_5 , at ~ 51 Oe for $x = 1.0\text{wt}\%$ V_2O_5 , and at $\sim 53.89\text{Oe}$ for $x = 1.5\text{wt}\%$ V_2O_5 , respectively. Beyond these applied field for different compositions, the magnetization increase slowly and then samples becomes saturated. These results confirmed that all samples have shown the typical magnetic hysteresis characteristic with soft nature ferrite [15].

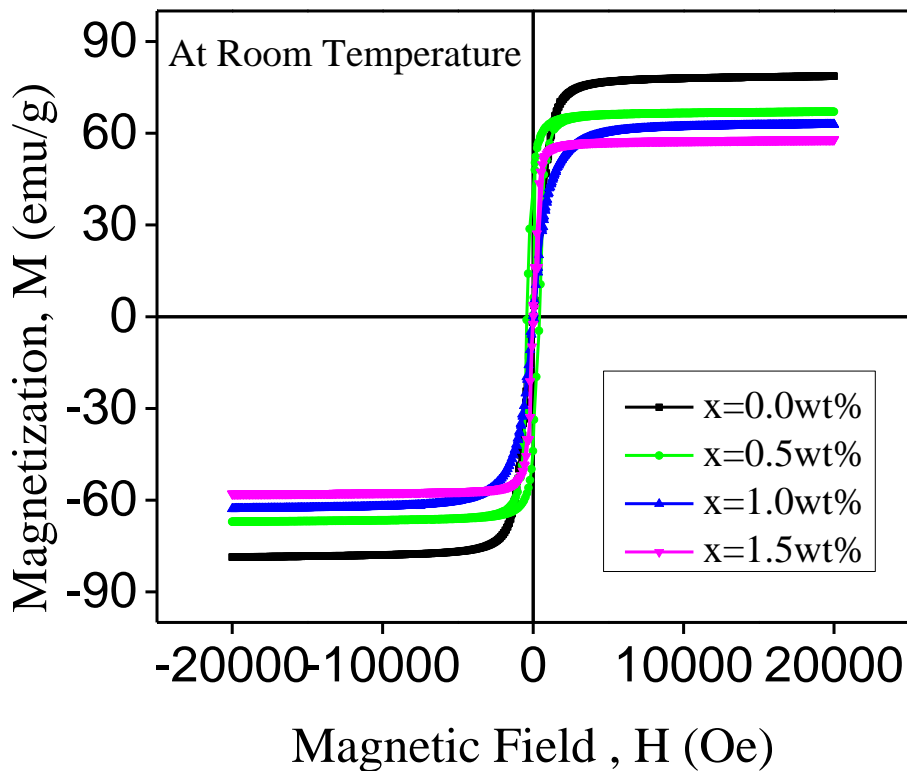


Fig.4.9 Variation of magnetization (M) with the applied magnetic field (H).

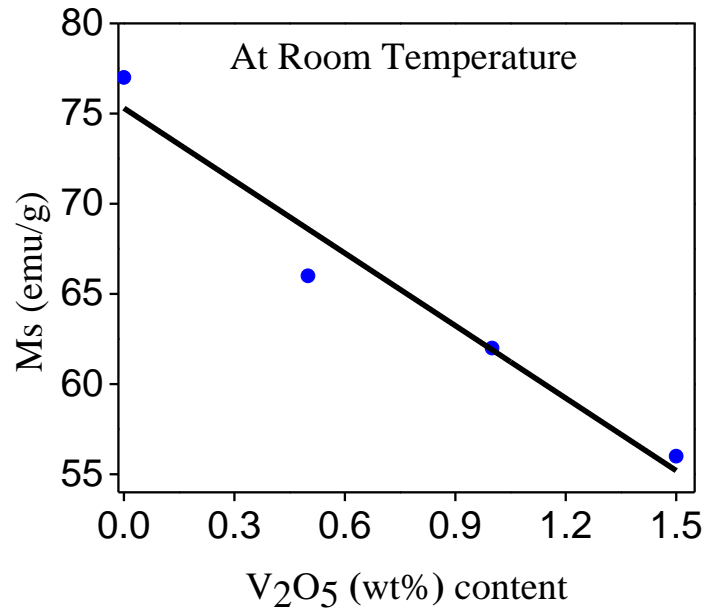


Fig.4.10 Variation of saturation magnetization (M_s) with V_2O_5 (wt%) contents.

Fig.4.10 shows the variation of saturation magnetization (M_s) with the additive V_2O_5 (wt%) contents. It can be seen that the saturation magnetization decreases with increasing V_2O_5 concentration. This behavior can be explained as follows. The magnetic moment arises from the anti-parallel uncompensated electron spin between tetrahedral or A-sites and Octahedral or B-sites. There are three types of interactions present in the spinel ferrite system such as A-A, B-B and A-B exchange interaction. According to Néel's molecular field model [41], $J_{A-B} \gg J_{B-B} \gg J_{A-A}$, where, J_{A-B} = the super exchange interaction between A and B sites, J_{B-B} = B-B exchange interaction and J_{A-A} = A-A exchange interaction. As the V^{5+} ions increases, the relative number of Fe^{3+} ions decreases on both A and B sites, but the decrease on the B-sites is larger than that of the A sites. This will reduce the A-B exchange interaction. This decrease of A-B interaction is attributed to decrease of saturation magnetization with the amount of V_2O_5 contents.

The experimental magnetic moment was calculated according to following equation [39].

$$\mu_B = \frac{MM_s}{5585} \quad (4.1)$$

where M is the molecular weight of the sample and M_S the saturation magnetization. It is also observed that experimental magnetic moment (μ_B) decreases with the increase of V_2O_5 additive due to the reduction of A-B super exchange interaction. The experimental values of the magnetic moment are shown in Table 4.4.

Table 4.4 Experimental magnetic moment for different compositions at 300K.

Compositions	Experimental magnetic moment (μ_B) _{exp}
$Ni_{0.62}Co_{0.03}Zn_{0.35}Fe_2O_4$	3.38
$Ni_{0.62}Co_{0.03}Zn_{0.35}Fe_2O_4+0.5wt\% V_2O_5$	2.69
$Ni_{0.62}Co_{0.03}Zn_{0.35}Fe_2O_4+1.0wt\% V_2O_5$	2.75
$Ni_{0.62}Co_{0.03}Zn_{0.35}Fe_2O_4+1.5wt\% V_2O_5$	2.50

4.4.2 M-H curve at different Temperatures

The magnetization (M) as a function of applied magnetic field (H) for different compositions $Ni_{0.62}Co_{0.03}Zn_{0.35}Fe_2O_4 + xV_2O_5$ (where $x = 0.0, 0.5, 1.0, 1.5wt\%$) were also studied at different temperatures 300, 200, 100 and 4K. These are shown in fig.4.11. All the curves are represented the magnetic hysteresis behavior. It was found that the saturation magnetizations were increased due to decrease in temperatures. The exchange energy between sub-lattices in ferrites system was the responsible for the spontaneous alignment of dipoles. This can be explained on the basis of thermal energy. Due to decrease in thermal energy, the saturation magnetizations were increased by the alignment of dipoles [42]. The experimental magnetic moments are presented in fig.4.12 at different temperatures 300, 200, 100 and 4K. From these results, the experimental magnetic moments were decreased due to reduce of exchange interaction between tetrahedral and octahedral sites in spinel ferrites at the certain temperature.

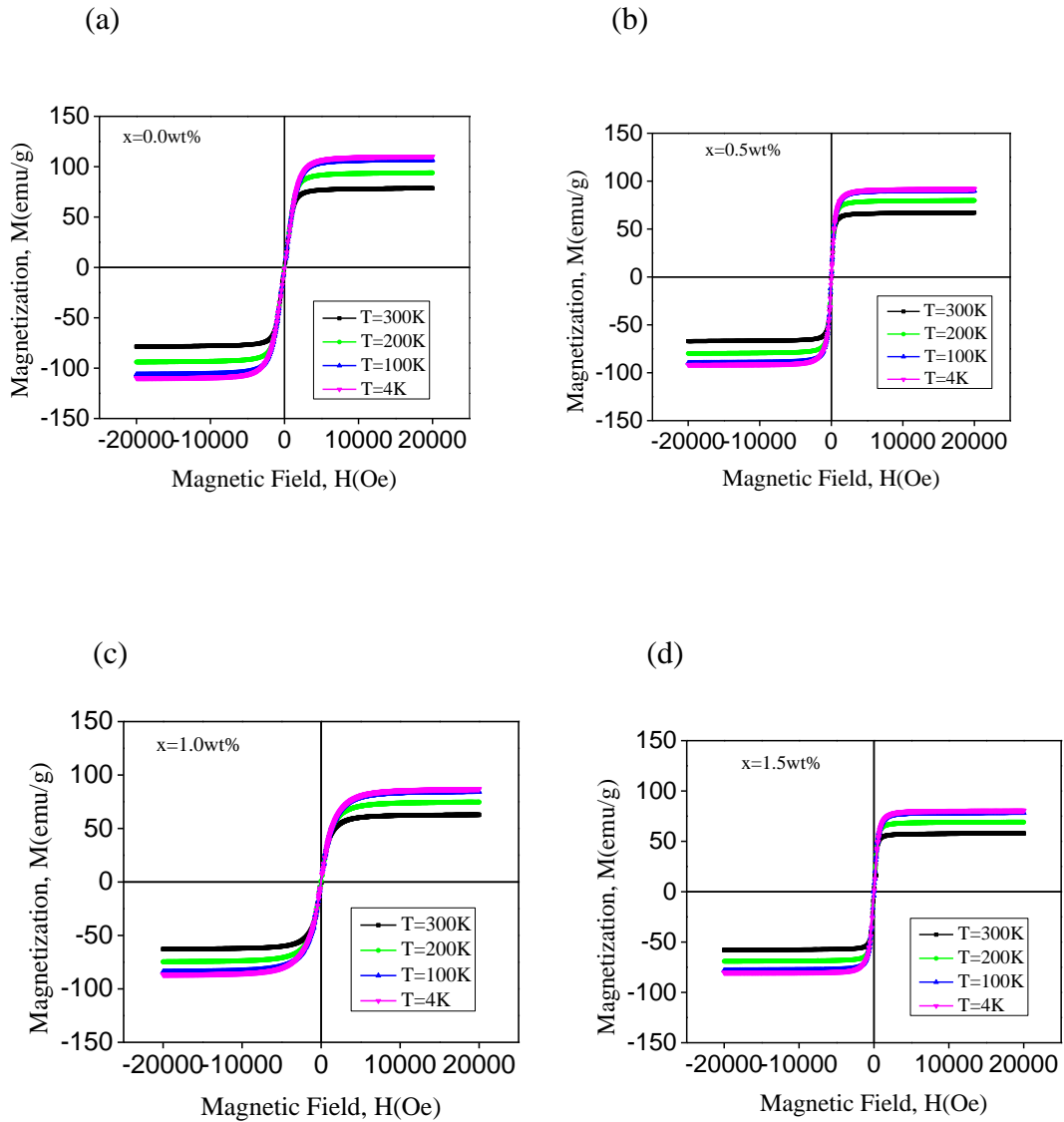


Fig.4.11 The magnetization (M) versus the applied magnetic field (H) curves at different temperatures for $\text{Ni}_{0.62}\text{Co}_{0.03}\text{Zn}_{0.35}\text{Fe}_2\text{O}_4 + x\text{V}_2\text{O}_5$, where a) $x=0.0\text{wt}\%$ V_2O_5 , b) $x=0.5\text{wt}\%$ V_2O_5 , c) $x=1.0\text{wt}\%$ V_2O_5 and d) $x=1.5\text{wt}\%$ V_2O_5 .

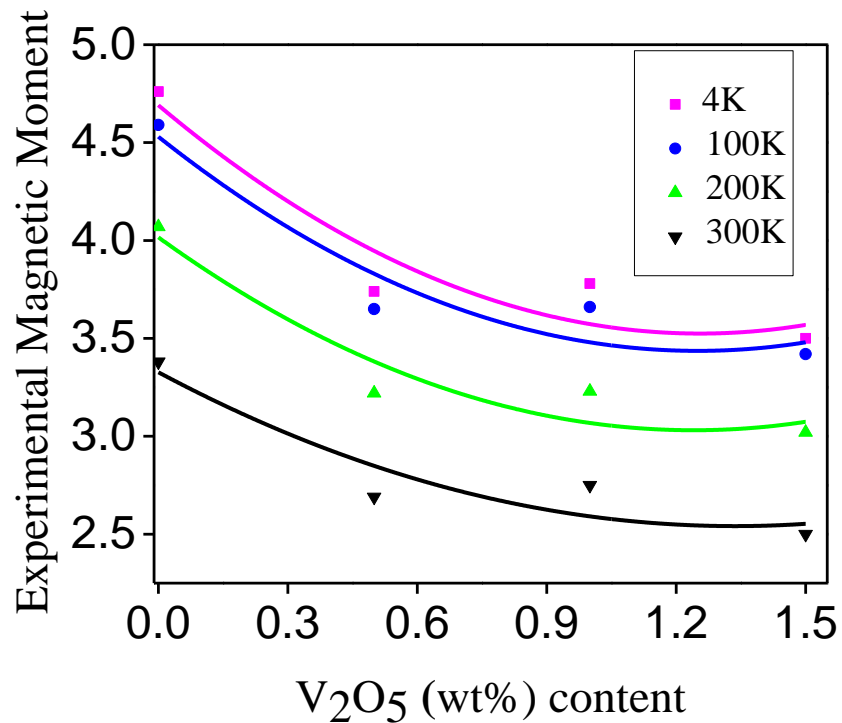


Fig.4.12 Experimental magnetic moment at different temperatures.

4.4.3 Curie Temperature

Curie temperature is a measure of exchange force in ferrimagnetism's. It is the temperature at which the thermal energy tends to disorder of the magnetic system. At this temperature, ferrimagnetic substance changes to a paramagnetic substance. In order to determine the Curie temperature (T_C), the temperature dependent magnetization measurement was observed for all samples and these are presented in fig.4.13. Magnetization falls rapidly when the magnetic state of the ferrite samples changes from ferrimagnetic to paramagnetic. The sharp falling of M with temperature shows the degree of homogeneity for samples [43-44]. The Magnetization falls abruptly close near to the Curie temperature (T_C). Table 4.5 represents the variation of T_C with the amount of V_2O_5 additive. It is observed that T_C decreases with increasing of V_2O_5 additive due to reduce of the super-exchange interaction between A and B sites. From these figures it can be explained that the 1st order derivative curves became sharper and represent the soft ferrites nature.

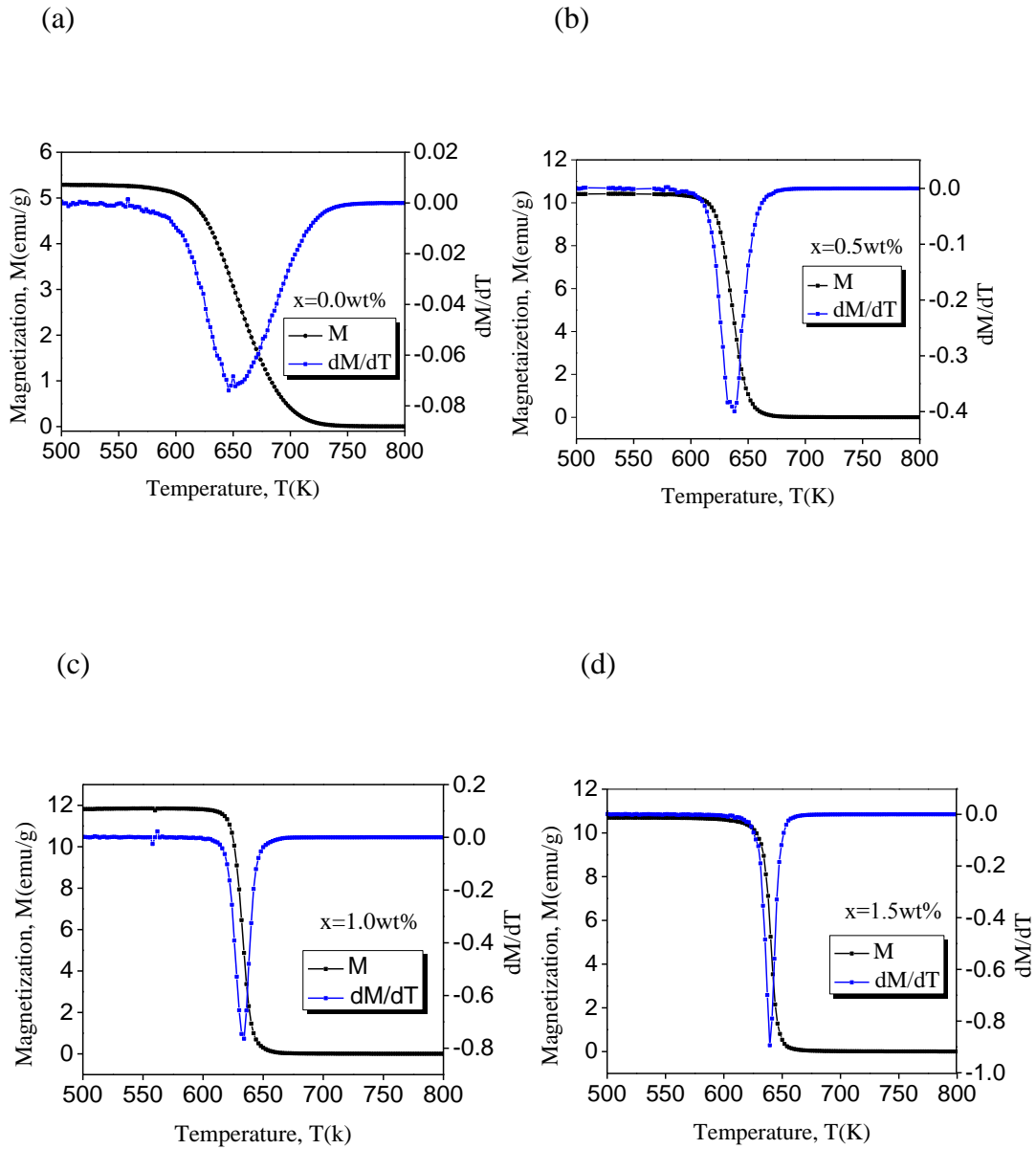


Fig. 4.13 Changes of Magnetization (M) and $\frac{dM}{dT}$ with temperature for a) $x=0.0\text{wt}\%$ V_2O_5 , b) $x=0.5\text{wt}\%$ V_2O_5 , c) $x=1.0\text{wt}\%$ V_2O_5 and d) $x=1.5\text{wt}\%$ V_2O_5 .

Table 4.5 Curie Temperature (T_C) for $\text{Ni}_{0.62}\text{Co}_{0.03}\text{Zn}_{0.35}\text{Fe}_2\text{O}_4 + x\text{V}_2\text{O}_5$ spinel ferrites.

Compositions	T_C (K)
$\text{Ni}_{0.62}\text{Co}_{0.03}\text{Zn}_{0.35}\text{Fe}_2\text{O}_4$	650
$\text{Ni}_{0.62}\text{Co}_{0.03}\text{Zn}_{0.35}\text{Fe}_2\text{O}_4 + 0.5\text{wt}\% \text{V}_2\text{O}_5$	636
$\text{Ni}_{0.62}\text{Co}_{0.03}\text{Zn}_{0.35}\text{Fe}_2\text{O}_4 + 1.0\text{wt}\% \text{V}_2\text{O}_5$	631
$\text{Ni}_{0.62}\text{Co}_{0.03}\text{Zn}_{0.35}\text{Fe}_2\text{O}_4 + 1.5\text{wt}\% \text{V}_2\text{O}_5$	638

4.5 Complex Permeability

The initial complex permeability can be written by $\mu^* = \mu' - i\mu''$, where μ' and μ'' are the real and imaginary parts of initial permeability, respectively. The real part μ' describes the stored energy expressing the component of magnetic induction \mathbf{B} in phase with the alternating magnetic field \mathbf{H} . The imaginary part μ'' describes the dissipation of energy expressing the component of magnetic induction \mathbf{B} out of phase with the alternating magnetic field \mathbf{H} [45]. The permeability can be expressed as [46].

$$\mu = 1 + \chi_{spin} + \chi_{dw} \quad (4.2)$$

where χ_{spin} is the susceptibility due to spin and χ_{dw} is the susceptibility due to domain wall motion. The dispersion of domain wall component depends on the square of the frequency and the spin rotational component is inversely proportional to the frequency. The domain wall motion contribution starts to decrease at the lower frequency and the spin rotational component decreases at relatively higher frequencies. According to Globus et al [47], the correlating among static susceptibility ($\mu_s - 1$), resonance frequency f_r , saturation magnetization (M_s) and grain diameter (D) are given as below:

$$(\mu_s - 1) = \frac{3M_s^2 4\pi D}{16E_w} \quad (4.3)$$

$$f_r = \frac{16E_w}{\pi\beta D^2} \quad (4.4)$$

where E_w is the wall energy and given by $E_w = K\delta w$, where K is the anisotropic energy and δw is the domain wall thickness, β = the domain wall damping factor.

According to this model, the larger grain size leads to high permeability and low resonance frequency. The smaller grain size leads to higher resonance frequency. As grain size increases, the multi domain grains are obtained which induces in higher permeability values due to the domain wall contribution. Thus, the domain wall motion is affected by the grain size and enhanced with the increase of grain size. Also an increase in the density of the V_2O_5 contents not only results in the reduction of demagnetizing field due to reduction of pores but also raises the spin rotational contribution, which in turn increases permeability. Fig 4.14 shows the variation of the real part of the permeability μ' with frequency for different composition sintered at 1200°C . The general characteristics of the curve in Fig.4.14 is that μ' remains fairly constant in the frequency range shown in the figure up to some critical frequency characterized by the onset of resonance. At these frequencies, after a small rise, the curves drop fairly rapidly to very smaller values. This phenomenon is called ferrimagnetic resonance. This trend of the curve is clearly visible for all samples. The resonance frequency peaks are the result of the absorption of energy due to the matching of the oscillation frequency of the magnetic dipoles and the applied frequency. The initial magnetic permeability for $Ni_{0.62}Co_{0.03}Zn_{0.35}Fe_2O_4 + 1.5\text{wt}\% V_2O_5$ is highest in compare to other compositions. This is because the sintered density is highest and the porosity is lowest for this composition. This high permeability ferrite can be used in high quality coils as a core only in a limited frequency range. The variation of imaginary part of the initial permeability μ'' with frequency for samples of different compositions is shown in fig.4.15. It was found that the rise in permeability is associated with the rise in loss represented by μ'' . The variation of relative quality factor (RQF) with the applied frequency of the studied composition is illustrated in fig.4.16. RQF increases with the increase in frequency showing a peak, after that decreases with further increase in frequency. It was found that the RQF enhanced due to increase of V_2O_5 additive in Ni-Co-Zn ferrites. The maximum RQF was obtained for $0.5\text{wt}\% V_2O_5$ in compare to other compositions.

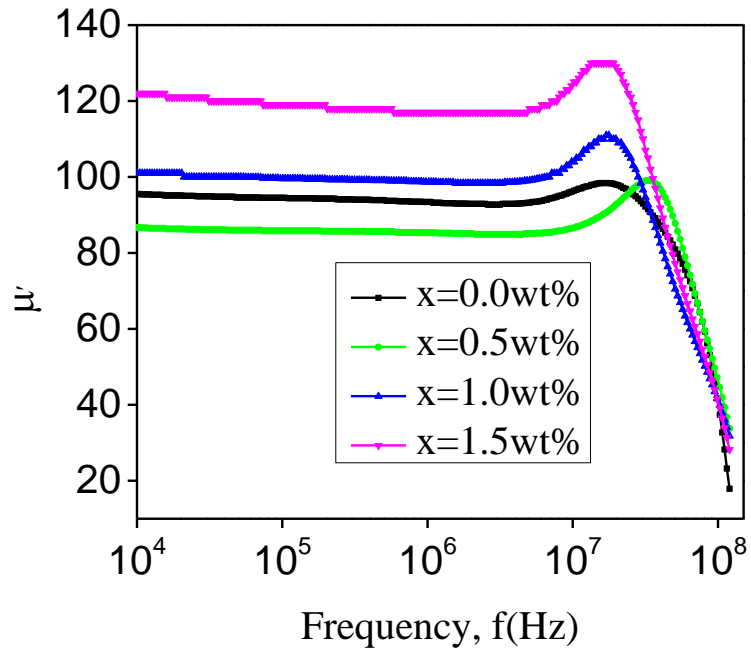


Fig.4.14 Variation of the real part of the initial permeability with frequency.

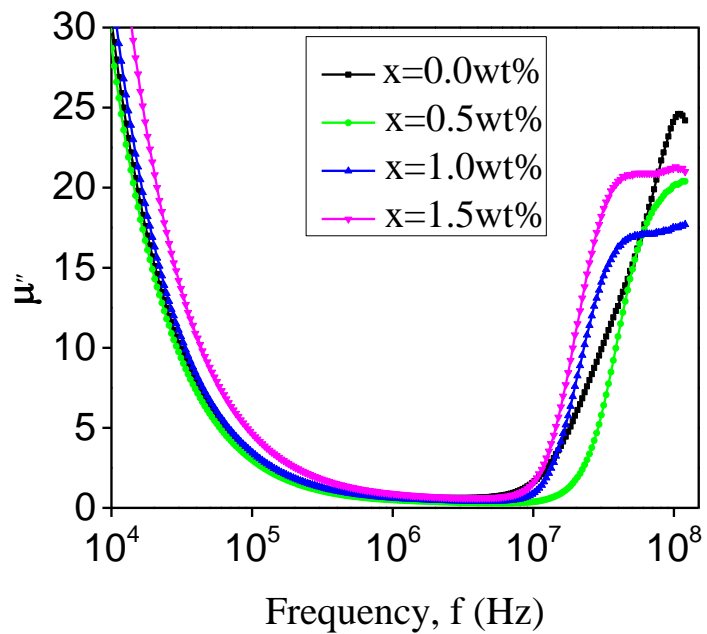


Fig.4.15 Variation of the imaginary part of the initial permeability with frequency.

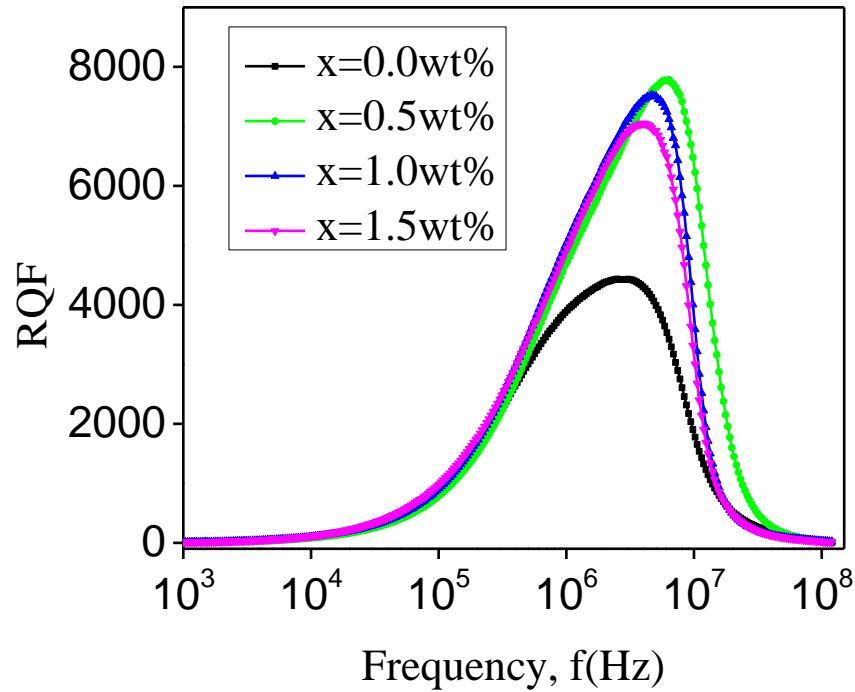


Fig.4.16 Variation of Relative Quality Factor (RQF) with frequency

4.6 Electrical Properties

4.6.1 Dielectric Constant

The variations of real (ϵ') and imaginary (ϵ'') parts of dielectric constant of $\text{Ni}_{0.62}\text{Co}_{0.03}\text{Zn}_{0.35}\text{Fe}_2\text{O}_4 + x\text{V}_2\text{O}_5$ compositions with applied frequency at room temperature are shown in fig.4.17 and fig 4.18, respectively. It can be seen that both cases dielectric constants were decreased with increasing of frequency. The dielectric constant is larger for the sample $x = 0.0\text{wt}\%$ V_2O_5 in comparing to $x = 0.5\text{-}1.50\text{wt}\%$ V_2O_5 added samples at the lower frequency. At certain frequency which is called critical frequency, dielectric constant remains constant with applied frequency. This is because the electron exchange interaction $\text{Fe}^{2+} \leftrightarrow \text{Fe}^{3+}$ cannot follow the applied field due to the phase delay to line up their axes parallel with the field direction. The dielectric property of the sample follows Maxwell-Wagner type interfacial polarization [48] and shows heterogeneous structure of the dielectric materials. The dielectric materials show that it has two-layer formation,

where the first layer is formed by large ferrites grains of clearly good conducting materials which are separated by relatively poor conducting substances of the second thin layer (grain boundaries). At high frequencies, the ferrites grain is more efficient while the grain boundaries are more effective at low frequency. This was found in this study ferrite samples. When an external electric field is applied on the dielectric medium, the charge carriers initiate to migrate through the conducting grain and are aggregate at the resistive grain boundary. Because of high dielectric constant, large polarization took place within the dielectric medium. At low frequencies, the thin conduction grain boundaries participate to forming the region, which gives a high value of permittivity due to different types of polarization mechanism. In the low-frequency region, all of the four types of polarization mechanisms (ionic, electronic, dipolar, and space-charge polarization) contribute to the total polarization in the compound resulting in high dielectric constant.

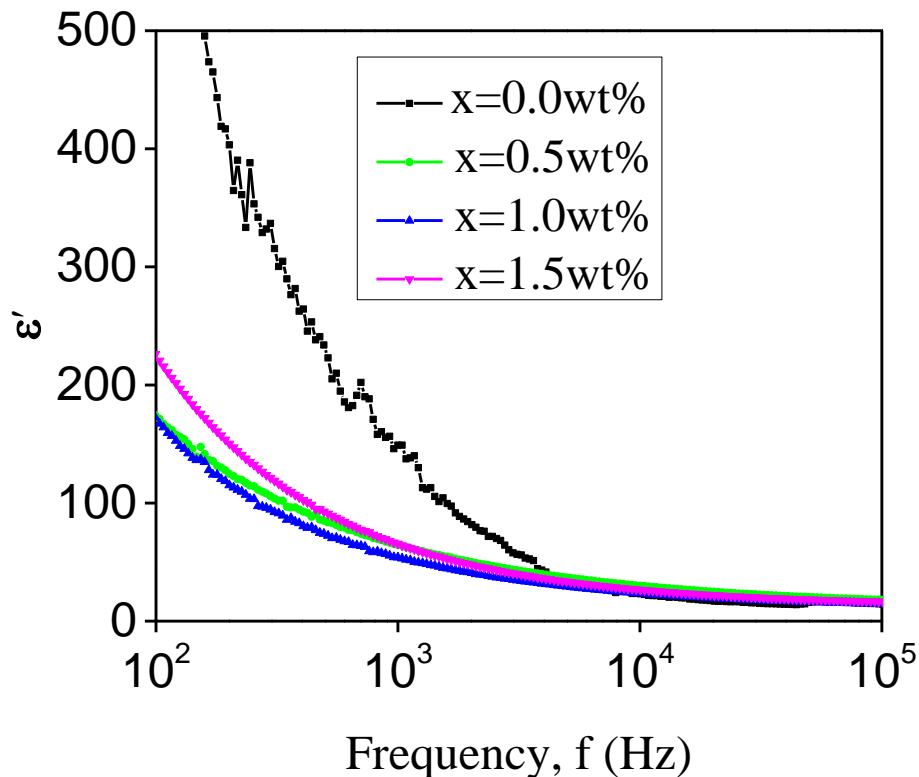


Fig.4.17 Variation of real part of the dielectric constant with frequency.

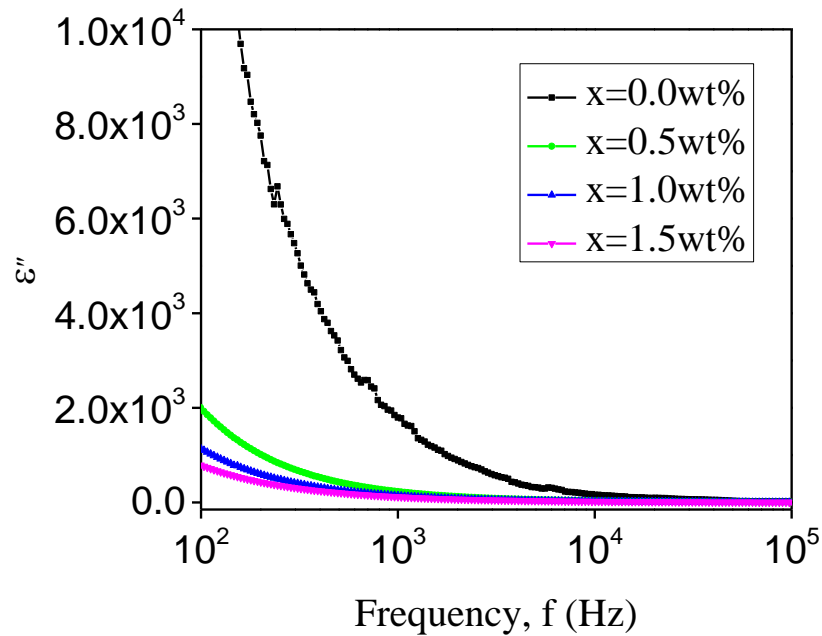


Fig.4.18 Variation of imaginary part of the dielectric constant with frequency.

4.6.2 Dielectric Loss tangent

Dielectric loss quantifies a dielectric material's inherent dissipation of electromagnetic energy as a form of heat. There are two types of loss in the dielectric medium. In conduction loss, the energy dissipation caused by flowing of charge through a material. On the other hand, in dielectric loss, the dissipation of energy caused by the movement of charges in an alternating electromagnetic field as polarization switches direction [49]. Generally, the higher dielectric loss is shown by the materials, which have higher dielectric constant. Dielectric loss factor ($\tan\delta$) of $\text{Ni}_{0.62}\text{Co}_{0.03}\text{Zn}_{0.35}\text{Fe}_2\text{O}_4 + x\text{V}_2\text{O}_5$ as a function of frequency is shown in fig 4.19. From this figure, it is found that at low-frequency region, the dielectric loss factor is high because more energy requires for the charge carries in the hopping process. At high frequencies, the conducting grains are more efficient due to low energy is necessary for the hoping mechanism of the charge carriers. The alignment of a dipole is not an instantaneous phenomenon these dipoles take some time to align with the field. This is called dipole relaxation. When the relaxation or

resonance frequency is equal to the applied frequency, a maximum in loss tangent may have occurred.

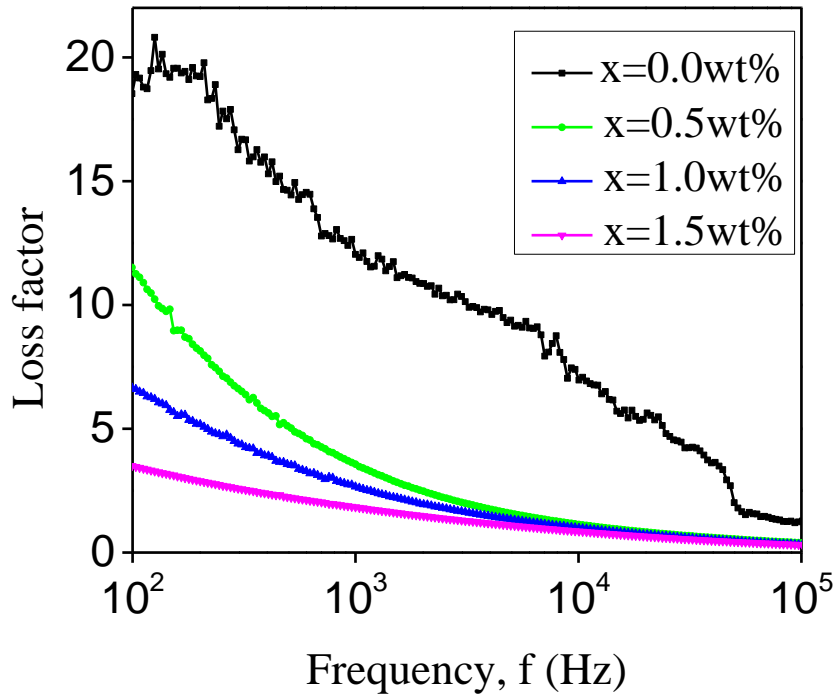


Fig.4.19 Variation of Loss factor as a function of frequency.

4.6.3 AC Resistivity

Fig.4.20 shows the variation of electrical resistivity, ρ with the frequency of $\text{Ni}_{0.62}\text{Co}_{0.03}\text{Zn}_{0.35}\text{Fe}_2\text{O}_4 + x\text{V}_2\text{O}_5$ at room temperature. It shows that the resistivity decreases with increasing of frequency. It can be also seen that the resistivity is found to be maximum for $x = 1.5\text{wt}\%$ V_2O_5 . The most probable conduction mechanism is electron hopping between Fe^{2+} and Fe^{3+} ions $\text{Fe}^{2+} \leftrightarrow \text{Fe}^{3+} + e^-$. This process is expected to take place between two adjacent octahedral sites in the spinel lattice [50].

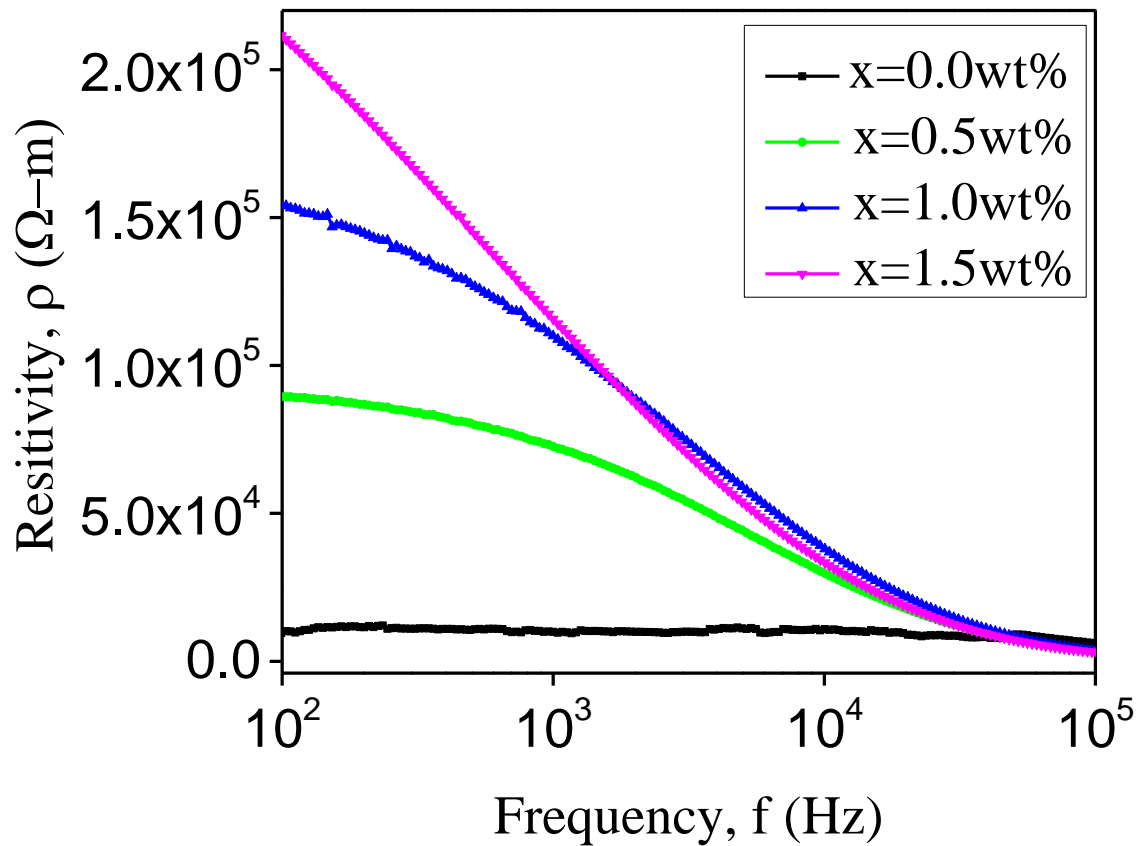
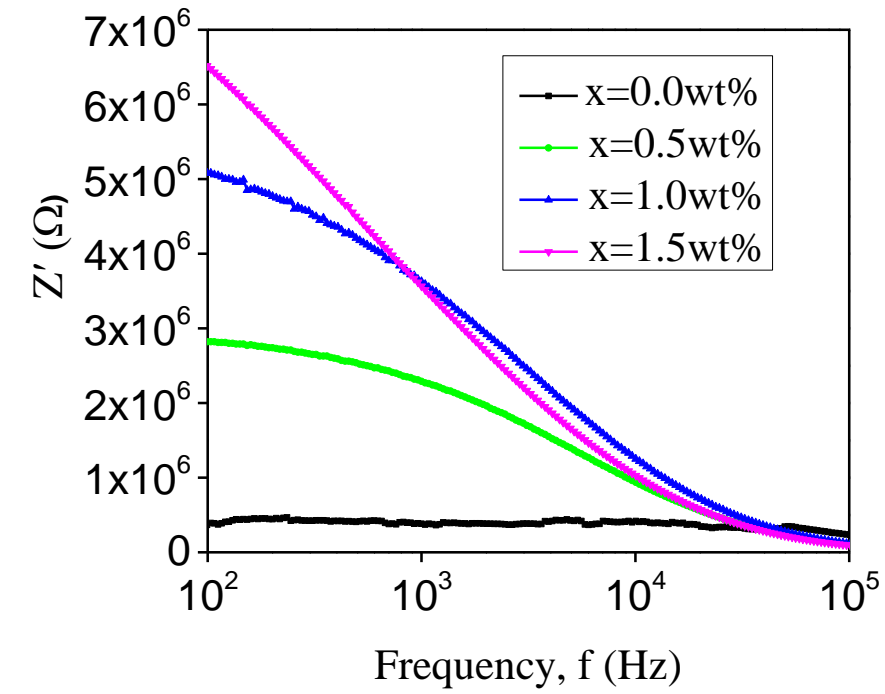


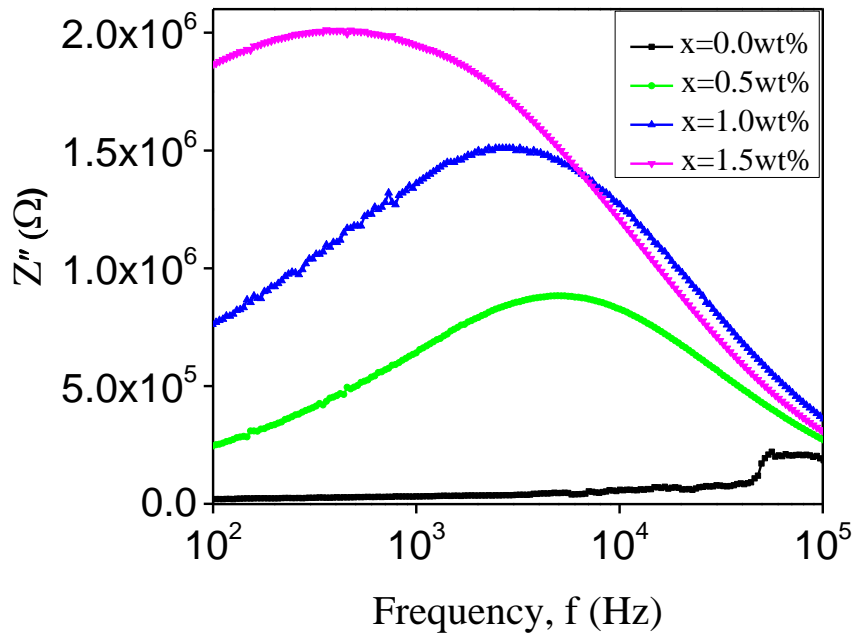
Fig.4.20 Variation of Resistivity with frequency.

4.6.4 Complex Impedance Spectroscopy

Complex impedance spectroscopy (CIS) is a very important path for distinguishing the electrical properties of materials [51]. Fig.4.21 shows the frequency dependent real (Z') and imaginary (Z'') parts of the impedance for $\text{Ni}_{0.62}\text{Co}_{0.03}\text{Zn}_{0.35}\text{Fe}_2\text{O}_4 + x\text{V}_2\text{O}_5$ at 1200°C sintering temperature. It is from Fig.4.21 (a) that the value of Z' decreases sharply up to 100 KHz and at high frequency region it becomes constant. This indicates that the value of conductivity increases with increasing of frequency.



(a)



(b)

Fig.4.21 Variation of (a) Z' and (b) Z'' as a function of frequency.

The higher value of Z' in the low frequency region that means the polarization is high at low frequency region. So, it is noticed that all kinds of polarization are present in low frequency region. However, under the influence of high frequency external applied field region the plateau like behavior of Z' implies likely incident of space charge polarization. The imaginary part of impedance Z'' shows similar behavior as $Z' < 1$ KHz frequency region.

CHAPTER 5 CONCLUSIONS

$\text{Ni}_{0.62}\text{Co}_{0.03}\text{Zn}_{0.35}\text{Fe}_2\text{O}_4 + x\text{V}_2\text{O}_5$ (where $x = 0.0, 0.5, 1.0, 1.5\text{wt}\%$) spinel ferrites have been successfully synthesized by using standard solid state reaction method. The effect of V_2O_5 addition on the structural, magnetic and electrical properties of Ni-Co-Zn ferrites having the compositions $\text{Ni}_{0.62}\text{Co}_{0.03}\text{Zn}_{0.35}\text{Fe}_2\text{O}_4 + x\text{V}_2\text{O}_5$ (where $x = 0.0, 0.5, 1.0$ and $1.5\text{wt}\%$) are reported. The XRD patterns confirmed a cubic spinel structure for all the samples. From the XRD results, it was found that the lattice parameters were slightly decreased with the increase of amounts of V_2O_5 (wt%) contents. The X-ray density (ρ_x) and bulk density (ρ_B) were increased due to the addition of V_2O_5 . It was found that both ρ_x and ρ_B increased with increasing amount of V_2O_5 contents. In this observation, ρ_x was always higher than that of ρ_B with V_2O_5 addition, which may be attributed to the existence of pores. The value porosity of the samples ($P\%$) were found to decrease with increasing of V_2O_5 contents, which clearly demonstrates the role of V_2O_5 as sintering aid to enhance densification of the ferrite samples.

By using the linear intercept method, the average grain size of all the samples were calculated from surface electron microscopy (SEM). It is noticed from the microstructure that V_2O_5 addition has substantial role in the growth of grains sintered at $T_S = 1200^\circ\text{C}$. A four times increase of grain size from $1.5\ \mu\text{m}$ for the sample $x = 0.0\ \text{wt}\%$ V_2O_5 to $6.8\ \mu\text{m}$ for that of $x = 1.5\ \text{wt}\%$ V_2O_5 is evident. The effect of V_2O_5 on the sintering mechanism and grain growth is clearly reflected from this study. This has been reflected in the increase of density or decrease of porosity with the addition of V_2O_5 .

From the magnetic hysteresis measurement for the all samples, it is clearly observed that the saturation magnetization (M_S) and the number of experimental Bohr magneton (μ_B) at room temperature are decreased with increasing of V_2O_5 (wt%) contents. The decrease of saturation magnetization can be attributed to the reduction of A-B super exchange interactions in the spinel lattices. Introduce of V_2O_5 into Ni-Co-Zn ferrites, i.e. with the increase of V^{5+} ions, the relative number of Fe^{3+} ions decreases on both A and B sites, but the decrease on the B-sites is larger than that on the A sites. This will reduce the A-B exchange interaction.

The magnetization, M as a function of applied magnetic field, H for different compositions $\text{Ni}_{0.62}\text{Co}_{0.03}\text{Zn}_{0.35}\text{Fe}_2\text{O}_4 + x\text{V}_2\text{O}_5$ (where $x = 0.0, 0.5, 1.0, 1.5\text{wt}\%$) were studied at different temperatures 300, 200, 100 and 4K. The exchange energy between sub-lattices in ferrites are the responsible for the spontaneous alignment of dipoles. This can be explained on the basis of thermal energy. Due to decrease of the thermal energy, the saturation magnetizations were increased by the alignment of dipoles. In order to determine Curie temperature (T_c), the temperature dependent magnetization was observed for all samples. It is observed that T_c decreases with increasing of V_2O_5 additives due to reduce of the super-exchange interaction between A and B sites.

The complex permeability measurement shows that the values of initial permeability were increased with increasing of the amount of additives; V_2O_5 because of the domain wall energy was decreased with additive as a result the initial permeability (μ') is increased. It was found that the relative quality factor (RQF) enhanced due to increase of V_2O_5 additive in Ni-Co-Zn ferrites. The maximum RQF was obtained for 0.5wt% V_2O_5 in compare to other compositions.

The frequency dependent dielectric constant (ϵ) was measured at room temperature in the frequency range 20Hz to 120Hz. It can be seen that both cases dielectric constants were decreased with increasing of frequency. The dielectric constant is larger for the sample $x = 0.0$ wt% V_2O_5 in comparing to $x = 0.5-1.5$ wt% V_2O_5 added samples at the lower frequency. At certain frequency which is called critical frequency, dielectric constant remains constant with applied frequency. This is because the electron exchange interaction $\text{Fe}^{2+} \leftrightarrow \text{Fe}^{3+}$ cannot follow the applied field due to the phase delay to line up their axes parallel with the field direction. The dielectric property of the sample follows Maxwell-Wagner type interfacial polarization.

The electric resistivity, ρ of the experimental samples was increased with increasing of frequency and at higher frequency region it remains invariant. The most probable conduction mechanism is electron hopping between Fe^{2+} and Fe^{3+} ions, $\text{Fe}^{2+} \leftrightarrow \text{Fe}^{3+} + e^-$.

The electrical properties of materials could be distinguished by complex impedance spectroscopy analysis. The values of Z' and Z'' were indicated that the value of conductivity was higher in lower frequency region as well as the value polarization was also higher in lower frequency region. In higher frequency region, it has been shown plateau like behavior.

References

- [1] Raju, K., Venkataiah, G., Yoon, D. H., “Effect of Zn substitution on the structural and magnetic properties of Ni-Co ferrites”, *Ceram. Int.*, vol. 40, pp 9337–9344, 2014.
- [2] Satyanarayana, G., Rao, N., Babu, K. V., “Structural, dielectric and magnetic properties of Al^{3+} and Cr^{3+} substituted Ni-Zn-Cu ferrites., *J. Nanosci. Tech.*, vol. 4, pp 487-491, 2018.
- [3] Jahan, N., Khan, M.N.I., Chowdhury, F.U.Z., Akhter Hossain, A.K.M., Hoque, S.M., Matin, M.A., Hossain, M.N., Hossain, M.M., Uddin, M.M., ” Influence of Yb^{3+} on the structural, electrical and optical properties of sol-gel synthesized Ni-Zn nanoferrites” *Journal Pre-proofs.*, vol. 19, pp 1-12, 2020.
- [4] Huang, X., Zhang, J., Lai, M., and Sang, T., “Preparation and microwave absorption mechanisms of the Ni-Zn ferrite nanofibers” *J. Alloys Compd.*, vol. 627, pp 367–373, 2015.
- [5] Ghodake, J. S., Kambale, R. C., Salvi, S. V., Sawant, S. R. and Suryavanshi, S. S., “Electric properties of Co substituted Ni-Zn ferrites”. *J. Alloys Compd.*, vol. 486, pp 830–834, 2009.
- [6] Huq, M. F., Saha, D. K., Ahmed, R., Mahmood, Z. H., “ Ni-Cu-Zn Ferrite Research: A Brief Review” *J. Sci. Res.*, vol. 5, pp 215-233, 2013.
- [7] Mirzaee, O., Golozar, M. A., Shafyei, A., “Influence of V_2O_5 as an effective dopant on the microstructure development and magnetic properties of $\text{Ni}_{0.64}\text{Zn}_{0.36}\text{Fe}_2\text{O}_4$ soft ferrites,” *Materials Characterization*, vol. 59, pp 638-641, 2008.
- [8] Janghorban, K., Shokrollahi, H., “Influence of V_2O_5 addition on the grain growth and magnetic properties of Mn-Zn high permeability ferrites,” *Journal of Magnetism and Magnetic Materials.*, vol. 308, pp 238-242, 2007.
- [9] Herrera, G., Moreno, P.M.M., “Microstructure dependence of the magnetic properties of sintered Ni–Zn ferrites by solid-state reaction doped with V_2O_3 .” *J.Mater Sci.*, vol. 47, pp 1758-1766, 2012.
- [10] Rao, B. P., Caltun, O., Dumitru, I., Spinu, L. “Complex permeability spectra of Ni-Zn ferrites doped with $\text{V}_2\text{O}_5/\text{Nb}_2\text{O}_5$ ” *Journal of Magnetism and Magnetic Materials.*, vol.

- 308, pp 238-242, 2007).
- [11] Kaiser, M., "Influence of V_2O_5 ion addition on the conductivity and grain growth of Ni-Zn-Cu ferrites" *Current Applied Physics.*, vol. 10, pp 975-984. 2010.
- [12] Ghodake, J. S., Kambale, R. C., Salvi, S. V., Sawant, S. R. and Suryavanshi, S. S., "Magnetic and microwave absorbing properties of Co^{2+} substituted nickel-zinc ferrites with the emphasis on initial permeability studies." *J. Mang. Mang. Mater.*, vol. 401, pp 938-942, 2016.
- [13] Patil. M. S., Kale. C. M., Babrekar. M. K., Pandit. A. A., Shingule., "Effect of V_2O_5 Addition on Electrical and Dielectric Properties of Ni-Zn ferrite." *IARJSET.*, vol. 4, pp 58-62, 2017.
- [14] Lebourgeois, R., Duguey, S., Ganne, J. P., Heintz, J. M., "Influence of V_2O_5 on the magnetic properties of nickel-zinc-copper ferrites," *J Magn. Magn. Mater.*, vol. 312, pp 328-330, 2007.
- [15] Mirzaee, O., Shafyei, A., Shokrollahi, H., "Influence of MoO_3 and V_2O_5 co-doping on the magnetic properties and microstructure of a Ni-Zn ferrite", *Journal of Alloys and Compounds.*, vol. 461, pp 312-315, 2008.
- [16] M. A. Wahab, Solid State Physics: Structure and Properties of Materials, Narosa Publishing House, New Delhi 1999.
- [17] Goldman, A., Handbook of Modern Ferromagnetic Materials, Kulwer Acad. Pub, Boston, U.S.A, 1999.
- [18] Cullity, B.D., Introduction to Magnetic Materials, Addison-Wisley Publishing Company, Inc., California, 1972.
- [19] Valenzuela, R., Magnetic Ceramics, Cambridge University Press, Cambridge, 1994.
- [20] Brailsford, F., Physical Principles of Magnetism, D. van Nostrand Company Ltd., London, 1996.
- [21] Saxena, B. S., Gupta, R. C., Fundamental of Solid State Physics, Pragati Laser Type Ltb., Delhi, 2000.
- [22] Prodromakis, T., Application of Maxwell-Wagner Polarization in Monolithic Technologies, pp 25-26, 2008.
- [23] "Nickel-Oxide" Wikimedia Foundation, 21 Nov, 2019, en. [Wikipedia.org/wiki/Zinc-](https://en.wikipedia.org/wiki/Zinc-oxide)

oxide.

- [24] "Cobalt-Oxide" Wikimedia Foundation, 21 Nov, 2019, en. Wikipedia.org/wiki/cobalt-oxide.
- [25] "Zinc-Oxide" Wikimedia Foundation, 21 Nov, 2019, en. Wikipedia.org/wiki/zinc-oxide.
- [26] "Ferric-Oxide" Wikimedia Foundation, 21 Nov, 2019, en. Wikipedia.org/wiki/ferric-oxide.
- [27] "Vanadium-Oxide" Wikimedia Foundation, 21 Nov, 2019, en. Wikipedia.org/wiki/Vanadium-oxide.
- [28] Shah, M. R., "dielectric properties of alkaline earth (D = Ba, Sr, Ca) and rare earth (T= La, Nd) substituted polycrystalline $D_{1-x}T_x(T_{0.5}Fe_{0.5})O_3$ pervoskite", Ph. D. Thesis, Department of Physics, Bangladesh University of Engineering and Technology, 2013.
- [29] Hossain, A. K. M. A., "Investigation of colossal magneto resistance in bulk and thick film magnetites", Ph. D., Thesis Imperial College, London, 1998.
- [30] Brooks, R. J., Sintering: An Overview, Concise Encyclopedia of Advanced Ceramic Materials, Pergamon press, Oxford, pp. 438, 1998.
- [31] Reijnen, P., Science of Ceramics, Academic Press, London, 1967.
- [32] Slick, P. I., Ferrites for Non-microwave Applications, Vol. 2, North Holland Pub. Co., 1980.
- [33] Mazen, S. A. and Dawoud, H. A., "Structure and Magnetic Properties of Li-Cu ferrites", *Phys. Stat. sol.*, vol. 172, pp 275-289, 1999.
- [34] Kingery, W. D., Bowen, H. K., and Uhlman, D. R., Introduction to Ceramics, 2nd edition, Wiley Interscience, Newyork, pp. 476, 1976.
- [35] Kittel, C., Introduction to Solid State Physics, 7th edition, Jhon Wiley & Sons, Inc., Singapore, 1996.
- [36] Chikazumi, S., Physics of Magnetism, Jhon Wiley & Sons, Inc., New York , 1966.
- [37] Macdonald, J. R. Impedance Spectroscopy. Wiley, New York, 1987.
- [38] Goldman, A., Handbook of Modern Ferromagnetic Materials, Kulwer Acad. Pub, Boston, U.S.A., 1999.

- [39] Smith, J., Wijn, H. P. J., Ferrites, Wiley, New York, 1959.
- [40] Hossain-Zadeh, M., Mirzaee, O., "Synthesis and Characterization of V₈C₇ nanocrystalline powder by heating milled mixture of V₂O₅, C and Ca Via mechanochemical activation", *Advanced Powder Technology.*, vol. 25, pp 978-982, 2014.
- [41] Neel, L., *Annales de Physique (Paris)* 3, 137, 1948.
- [42] Bragg, B. J.W., Dickens, J., Neuber, A., "Investigation Into the Temperature Dependence of Ferrimagnetic Nonlinear Transmission Lines", *IEEE Transactions on Plasma Science.* Vol. 40, pp 2457-2461, 2012.
- [43] Cedillo, E., Ocampo, J., Rivera, V., and Valenzuela, R., "An apparatus for the measurement of initial magnetic permeability as a function of temperature", *Journal of Physics F: Scientific Instrument.*, vol. 13, pp 383, 1980.
- [44] Valenzuela, R., "A sensitive method for the determination of the Curie temperature in ferrimagnets", *Journal of Material Science*, vol. 15, pp 31-37, 1980.
- [45] Kong, L. B., Li, Z. W., Lin, G. Q., Gan, Y. B., "Ni-Zn Ferrites Composites with Almost Equal Values of Permeability and Permittivity for Low-Frequency Antenna Design", *IEEE Transactions on Magnetics.*, vol. 43, pp 6-10, 2007.
- [46] Rezlescu, E., Sachelaria, L., Popa, P. D., Rezlescu, N., "Effect of Substitution of Divalent Ions on the Electrical and Magnetic Properties of Ni-Zn-Me Ferrites", *IEEE Transactions on Magnetics.*, vol. 36, pp 3962-3967, 2000.
- [47] Glubus, A. and Duplex, P. "Size of bloch wall and parameters of the magnetic susceptibility in ferromagnetic spinels and garnets, *Phys. Stat. Sol. A.*, vol. 31, pp 765, 1969.
- [48] Maxwell, J., *Electricity and Magnetics*, vol. 1, section 328, Oxford University Press, London, 1873.
- [49] Koops, C. G., "On the dispersion of resistivity and dielectric constant of some semiconductors at audio frequency," *phys. Rev.*, vol. 83(1), pp. 121, 1951.
- [50] Folkmann, G., Hatem, G., Fehrmann, R., Gaune-Escard, M., Bjerrum, N., "Complex formation of pyrosulfate melts. 4. Density, potentiometry, calorimetry, and conductivity of the systems cesium pyrosulfate-vanadium pentaoxide, Cs₂S₂O₇-

- cesium sulfate and $\text{Cs}_2\text{S}_2\text{O}_7\text{-Cs}_2\text{S}_2\text{O}_4\text{-V}_2\text{O}_5$ in the temperature range 340-550. Degree. C”, *Inorganic Chemistry*, vol. 32, pp 1559-1565, 1993.
- [51] Omari, L. H., Moubah, R., Boutahar, A., Haiji, L., Ouatib, R. E., “Analysis of electrical properties using complex impedance spectroscopy in solid solutions $(\text{PbTiO}_3)_{0.97}\text{-(LaFeO}_3)_{0.03}$ prepared by sol-gel technique”, *Journal of Electroceramics*, vol. 44, pp 23-31, 2020.

Appendices

1. M. F. Uddin, S. M. Hoque, M. A. Hakim and M. S. Ullah, “Structural and Magnetic Properties of V_2O_5 added Ni-Co-Zn Ferrites”, *National Conference on Electronics and Informatics*, Atomic Energy Centre, Dhaka, 4-5 December, 2019.
2. M. F. Uddin, M. A. Hakim, J. Podder and M. S. Ullah, “Complex Permeability Studies of V_2O_5 Added Ni-Co-Zn Ferrites”, *International Conference on Physics-2020*, Atomic Energy Centre, Dhaka, 05-07 March, 2020.